Available online at www.sciencedirect.com
ScienceDirect
Icarus 194 (2008) 575–596
ICARUS
www.elsevier.com/locate/icarus

An improved crustal magnetic field map of Mars from electron reflectometry: Highland volcano magmatic history and the end of the martian dynamo

Robert J. Lillis [a,*], Herbert V. Frey [b], Michael Manga [c], David L. Mitchell [a], Robert P. Lin [a], Mario H. Acuña [b], Stephen W. Bougher [d]

[a] *UC Berkeley Space Sciences Laboratory, 7 Gauss Way, Berkeley, CA 94720, USA*
[b] *NASA Goddard Space Flight Center, Greenbelt, MD 20771, USA*
[c] *UC Berkeley Department of Earth and Planetary Science, Berkeley, CA 94720, USA*
[d] *University of Michigan Department of Atmospheric, Oceanic and Space Sciences, 2455 Hayward St., Ann Arbor, MI 48109-2143, USA*

Received 21 February 2007; revised 24 September 2007

Available online 23 December 2007

Abstract

We apply improved kinetic modeling of electron transport in the martian thermosphere to fit pitch angle distributions measured by the Mars Global Surveyor (MGS) Magnetometer/Electron Reflectometer (MAG/ER), together with appropriate filtering, binning, averaging and error correction techniques, to create the most reliable ER global map to date of crustal magnetic field magnitude at 185 km altitude, with twice the spatial resolution and considerably higher sensitivity to crustal fields than global maps of magnetic field components produced with MAG data alone. This map compares favorably to sparsely sampled dayside MAG data taken at similar altitudes, insofar as a direct comparison is meaningful. Using this map, we present two case studies. The first compares the magnetic signatures of two highland volcanoes, concluding that the comparatively greater thermal demagnetization at Syrtis Major compared with Tyrrhena Patera is likely due to a higher ratio of intruded to extruded magmas. The second uses the map along with topographic data to compare the magnetic signatures and crater retention ages of the demagnetized Hellas impact basin and magnetized Ladon impact basin. From this comparison, we determine that the martian global dynamo magnetic field went from substantial to very weak or nonexistent in the absolute model age time interval 4.15 ± 0.05 to 4.07 ± 0.05 Ga ago.

Keywords: Mars; Magnetic fields; Cratering; Mars, interior; Volcanism

1. Introduction

One of the most surprising results from the Mars Global Surveyor (MGS) mission was the discovery of very strong crustal remanent magnetism at Mars. The MGS Magnetometer (MAG) experiment measured crustal magnetic fields (Acuña et al., 1998) 10–20 times stronger at orbital altitudes than their strongest terrestrial counterparts (Connerney et al., 1999). This discovery, and the extensive analysis of MAG data which followed it, have succeeded in placing useful constraints upon the properties of the crustal magnetic sources responsible for these fields and upon the timing and orientation of the ancient dynamo-driven global magnetic field in which these sources were created (e.g. Acuña et al., 1999, 2001; Cain et al., 2003; Connerney et al., 1999, 2001; Hood et al., 2001, 2003, 2005; Arkani-Hamed, 2001a, 2001b, 2002a, 2002b, 2003, 2004, 2005; Arkani-Hamed and Boutin, 2004; Langlais et al., 2004; Purucker et al., 2000; Whaler and Purucker, 2005). However, the prime limiting factor in using the MAG data for interpreting these crustal sources is the altitude at which the vast majority of the data was collected, ∼400 km (Arkani-Hamed, 2004). Spatial resolution decreases linearly and sensitivity to crustal fields decreases by the 2nd to 3rd power with increasing altitude, making well-sampled lower altitude data very valuable for geophysical studies.

* Corresponding author.
E-mail address: rlillis@ssl.berkeley.edu (R.J. Lillis).

0019-1035/$ – see front matter
doi:10.1016/j.icarus.2007.09.032

For these reasons of sensitivity and resolution and because it was never expected that Mars would have strong crustal magnetic fields, another instrument called the Electron Reflectometer (ER) was included in the payload, to be used in concert with MAG to measure the magnetic reflection of electrons caused by the crustal fields and hence derive crustal field magnitudes nearer to the surface (Acuña et al., 1992), using a technique developed for measuring such fields at the surface of the Moon, known appropriately as 'Electron Reflectometry' (Anderson et al., 1976; Lin, 1979).

However, the ER data was not used for crustal field mapping until late 2002 (Lillis et al., 2003), 5 years into the mission, due to the unexpected strength of the crustal fields measured by MAG, the unexpectedly long elliptical orbit phase of the mission which gave almost 1000 low altitude MAG passes and because the theory of electron reflectometry in a planetary atmosphere had not previously been developed in sufficient detail. Now that those details have been worked out to the fullest practical degree (Lillis et al., 2008a), ER data can be used for its original purpose: the construction of a map of crustal magnetic fields which allows the interpretation of crustal magnetic features at a common altitude over the vast majority of the planet with a substantially lower threshold (4 nT at ∼200 km vs 8 nT at ∼400 km) and smaller spatial scale (factor of 2) than is possible with MAG alone.

An outline of the ER technique in its earlier form has already been published, to enable dissemination of early results (i.e. a preliminary partial map), by Lillis et al. (2004) but many details were omitted and some crucial aspects of the theory were not yet sufficiently understood. The technique was also summarized, again omitting many of the details, in Mitchell et al. (2007) (prepared in 2004–2005), for the purposes of concisely publishing the global ER magnetic map in its first form and geophysically interpreting some of the magnetic signatures. However, since the preparation of that manuscript, 33 additional months of data have been collected and understanding of the theory has matured substantially to the point where we can present full details of both the ER technique (in the companion article by Lillis et al., 2008a) and the construction of the final ER magnetic map ('final' because MGS was lost in November 2006), as well as some of the more interesting immediate conclusions we can draw from it (this article). The map presented in this article has 11 separate improvements from that published in Mitchell et al. (2007). These improvements will be discussed in Section 6.

In this paper, we outline the electron loss cone modeling, magnetic field parameterization and fitting techniques we use to solve for the crustal magnetic field magnitude at 185 km above the datum, correcting for the effects of parallel electric fields. We explain how a data set of ∼4 million of such measurements, over 3.75 martian years, is converted, using appropriate binning, filtering, averaging and error correction strategies, into the most accurate geographic map to date of crustal magnetic field magnitude at 185 km. We analyze the magnetic morphology and topology of the map, the statistical distribution of the crustal fields and formal uncertainties. Comparisons are made to published magnetic maps of Mars and a strategy for geophysical interpretation laid out. The map is then used to conduct two case studies. First, we analyze the magnetic signatures and surface geology/topography of the Syrtis Major and Tyrrhena Patera volcanoes to constrain aspects of their magmatic history. Second, we analyze the magnetic signatures and crater retention ages of the Hellas and Ladon impact basins to bracket the time during which the global magnetic field evolved from significant to weak or nonexistent. Readers primarily interested in the finished map and its geophysical application may skip Sections 2–4, 6, and Appendices A–G.

2. Fitting loss cones to observations to solve for crustal magnetic fields

Lillis et al. (2008a) describe in detail the theory of electron reflectometry in a planetary atmosphere, presenting a kinetic model of electron transport along open magnetic field lines (i.e. those connected to both the planetary crust and interplanetary magnetic field (IMF)), through an extended atmosphere, which predicts the shapes of loss cone pitch angle distributions at MGS mapping altitudes of ∼400 km. Parameters in this model which describe electrostatic potentials, magnetic field magnitude and atmospheric neutral density profiles between ∼400 km and the electron absorption region at ∼160–240 km, may be constrained by least-squares fitting to loss cones measured by MAG/ER (for examples, see Figs. 10 and 12 of Lillis et al., 2008a).

The model requires density profiles for the major molecular species of the martian atmosphere. We choose a reference atmosphere from the Mars Thermospheric Global Circulation Model (MTGCM) scaled (at all altitudes) to match the mean mass density derived at 185 km (the mean altitude of unity electron scattering depth) by Lillis et al. (2008b). Details of this model atmosphere may be found in Appendix A.

In order to use this model to solve for crustal magnetic fields, we parameterize the magnitude of the magnetic field (denoted B) as a function of distance along the field line to which the electrons are bound, by a constant term (the external, 'ambient' field, B_a) plus a crustal term that falls off as a power law (with exponent p) with distance z from the crust:

$$B(z) = B_a + (B_{sc} - B_a)\left(\frac{z_{sc}}{z}\right)^p, \tag{1}$$

where B_{sc} and z_{sc} are the field magnitude at the spacecraft and distance from the crustal source to the spacecraft respectively and where we assume a straight-line continuation of the field measured at the spacecraft at an angle θ to the horizontal. Anywhere on the planet, we expect p to be between 2 (exponent corresponding to an infinite line of dipoles) and 3 (the exponent for a single point dipole). In the strong crustal field region in the southern hemisphere, p has been measured as ∼2.2 (Brain et al., 2003).

Since B_{sc}, Z_{sc}, θ are directly measured quantities, Eq. (1) tells us that any combination of values of B_a and p uniquely determines the modeled magnetic field magnitude B at all altitudes. However, only magnetic field values in the electron absorption layer can affect the loss cone shape (Lillis et al.,

2008a). This layer ranges from ∼160 to 240 km altitude, depending on atmospheric variability, with the mean altitude of greatest sensitivity of loss cone shape with respect to crustal field magnitude (i.e. second term in Eq. (1)) occurring at 185 km altitude above the equipotential surface, known as the areoid, given by the 75th degree and order martian gravity model of Yuan et al. (2001). Details of sensitivity with respect to altitude may be found in Appendix B.

When the model is fitted to measured loss cones, the variables B_a and p are found to be highly correlated (i.e. the fitted value of the crustal field magnitude at 185 km, hereafter referred to as B_{185}, is constrained but there is no unique 'best' combination of B_a, p) because most of the electron absorption occurs over a narrow range of altitudes (25–40 km, see Fig. 15 of Lillis et al., 2008a). We can therefore choose the physically reasonable value for p of 2.5 and solve for the crustal field in terms of B_a/B_{sc}, (chosen because it conveniently ranges between 0 and 1). Electrostatic potentials modify the loss cones in an energy-dependent way while the effects of the magnetic profile are nearly energy-independent (Lillis et al., 2008a), so this potential can be simultaneously solved for along with B_{185} because we analyze pitch angle distributions in three adjacent energy channels (90–148, 148–245, 245–400 eV). We treat the electrostatic potential results as a correction to improve the accuracy of the B_{185} measurements since this article is primarily concerned with crustal magnetic fields. Details of the fitting procedure may be found in Appendix C.

3. Construction of crustal magnetic field map

We have almost 4 million individual nightside measurements of B_{185}, taken from April 1999 to June 2006 over most of the planet (except where the crustal magnetic field lines are permanently closed and loss cones never form; Lillis et al., 2004). We now employ appropriate filtering, binning, averaging and error correction techniques to construct from this data set the most accurate map possible of crustal magnetic field magnitude at 185 km altitude.

3.1. Geographic errors from straight field line tracing

We account for the shift in geographic location of these measurements from spacecraft altitude (∼400 km) to 185 km by assuming the field lines are straight over this distance. Errors come from measurement uncertainty of the magnetic field direction due to uncompensated spacecraft-generated fields, and from field line curvature. Analysis of these errors (explained in detail in Appendix D) shows that, by excluding all measurements with magnetic field magnitudes <10 nT and magnetic elevation angles <40°, the tracing error can be kept between 50 and 150 km for ∼98% of geographic regions. In the remaining areas, the crustal fields are so much stronger than external fields (30–50 nT on the dayside) that they have been adequately characterized near 200 km altitude by the MGS magnetometer (Acuña et al., 1999).

3.2. Filtering unreliable data

There are several reasons for certain measurements to be deemed unusable. First we wish to exclude all measurements taken while the spacecraft was in sunlight (solar zenith angle (SZA) $<\sim 120°$) because sunlight entering the instrument aperture contaminates the loss cones and because induced magnetic fields arising from the solar wind interaction with Mars' dayside ionosphere are generally smaller and less turbulent in the martian shadow compared with sunlit conditions (Ferguson et al., 2005). Magnetic gradients caused by such turbulence can cause magnetic reflection and hence mimic weak crustal magnetic fields. Loss cones from the terminator region ($90° <$ SZA $< 120°$) are analyzed for the purposes of atmospheric neutral density probing by Lillis et al. (2008b) because only regions with very strong crustal magnetic fields were considered, thus rendering the weak magnetic gradients caused by terminator magnetic turbulence negligible by comparison. We also exclude measurements with a χ^2 goodness-of-fit parameter greater than 2.0, a number determined by a visual inspection of a sample of the fits. After this filtering, ∼2.3 million reliable B_{185} measurements remain.

3.3. Correcting and fitting the data distributions

Our parameterization of the magnetic profile (Eq. (1)) necessarily assumes that the variable external and constant crustal components of the vector magnetic field can be added as scalar quantities (i.e. that they are co-linear), therefore B_{185} is a lower bound value for the true crustal field. By choosing only data from the side of the bimodal distribution of external field directions that gives the highest values of B_{185}, we limit ourselves to cases where the angle between the external and crustal fields is $<90°$. We then calculate the likely mean value of our underestimation as a function of magnetic field magnitude and add this amount appropriately to each measurement of B_{185}. Full details of this procedure are given in Appendix E.

The distribution of values of B_{185} in a given geographic region is best fit by the Weibull distribution (e.g. Johnson et al., 1995), a flexible, positive-only, two-parameter distribution. From any data distribution, the value of B_{185} we choose for the final map is the mode of the Weibull distribution that best fits that distribution. A full explanation of this fitting procedure is given in Appendix F.

3.4. Binning the data

For the purposes of geographic binning, we divide the planet up into almost equal-area 'rectangles' in longitude–latitude space: curved trapezoids in three dimensions. These are nearly perfect $0.5° \times 0.5°$ squares at the equator, while their longitude dimension increases poleward appropriately to ensure a nearly constant area (∼875 km^2) for all sectors. When assigning the most likely value of B_{185} to each sector, we consider all measurements within a 200 km-diameter circle centered the centroid of that sector. We 'scan' this circle across the planet,

using the Weibull fitting technique (Appendix F) to assign values of B_{185} to each sector, thereby producing a 'smoothed' map. Minimum crustal field wavelengths of ∼300 km were found using shorter binning intervals, giving a Nyquist wavelength of ∼150 km. This, combined with the typical tracing error for individual measurements of 50–100 km (Appendix D) makes binning intervals shorter than 200 km untrustworthy. Pixels with fewer than 10 measurements within their circle are ignored, and are shown in black in the maps in Figs. 1, 4, 6, 8. Such pixels make up 8.9% of the total map.

4. Primary analysis of crustal magnetic field map

Before any reliable interpretation of crustal magnetic field patterns can be made, it is useful to examine the data in untraced, unsmoothed, 'raw' map form to observe how derived crustal field magnitudes and data density vary on a global scale and to compare this to magnetic field maps measured directly at spacecraft altitude. Fig. 1 gives this comparison.

4.1. Loss cone formation probability and magnetic topology

The first thing we notice, by comparing Figs. 1A and 1B, is that loss cones form preferentially in regions where the magnetic field at spacecraft altitudes is mostly radial. This occurs in either of two instances. The first instance is in magnetic cusp regions, akin to earth's polar magnetic cusps but on a much smaller scale (i.e. the 'islands' of yellow and red surrounded by black in Fig. 1B), when the crustal magnetic field is strongly radial and so connects with the magnetotail field, allowing solar wind electrons to precipitate into the atmosphere (Lillis et al., 2004; Brain et al., 2006). The second instance is in certain weak field regions: Isidis (10° N, 85° E), east of Argyre (55° S, 345° E), southeastern Hellas (60° S, 75° E), Amazonis (∼30° N, ∼185° E), Elysium (25° N, 150° E) and most of Tharsis (∼10° N, ∼260° E). In these regions, the external induced magnetotail field is sufficiently radial to allow electron precipitation during at least some part of the martian year (Mars' obliquity causes the angle of the sunward/anti-sunward magnetotail field with respect to local horizontal to vary by ∼50° from perihelion to aphelion).

Measurements are much sparser near the poles because the nightside external field drapes around the planet (Bertucci et al., 2003), meaning that even during local winter near the north or south pole, the field is likely to be more horizontal than radial, inhibiting loss cone formation. Interestingly, though not as sparse as the polar regions, measurements are also relatively sparse and external fields are usually relatively horizontal over and to the west of the Utopia basin (40° N, 115° E), over the Hellas basin (42° S, 70° E) and over and to the west and southwest of the Argyre basin (50° S, 318° E). This longitudinal variation in weak field region loss cone formation probability is likely due to global magnetic topology differences caused by the strongest crustal fields' differing orientations with respect to the external, solar wind-induced field when the MGS spacecraft is in different geographic locations in its fixed orbit at 2 a.m. local time.

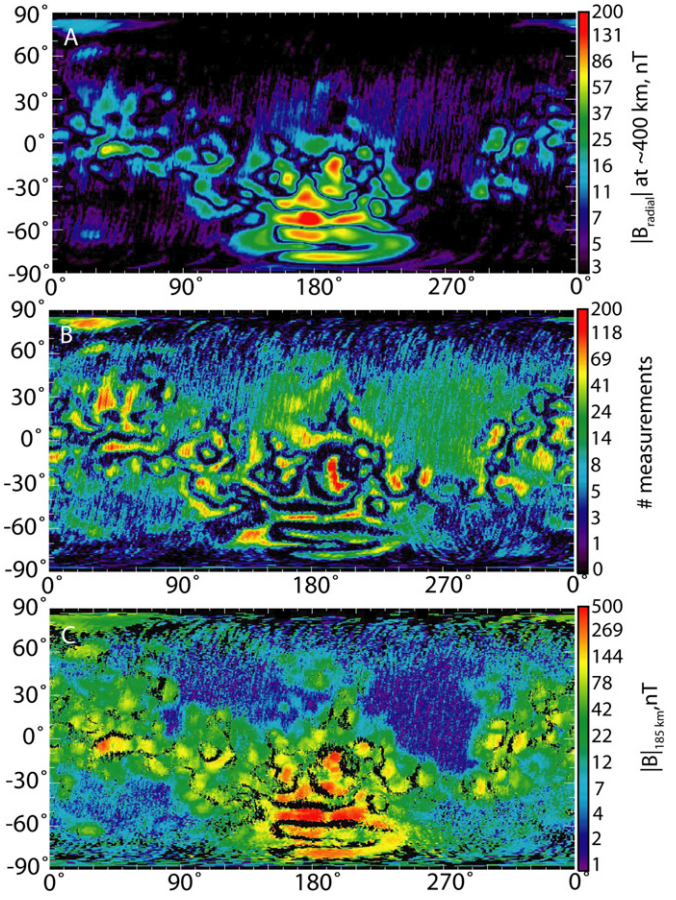

Fig. 1. Global cylindrical projection maps with respect to spacecraft position. Color scales are logarithmic. (A) shows the absolute value of the radial component of the total magnetic field measured at the spacecraft mapping orbit altitude (370–430 km) in 0.5° × 0.5° bins. (B) shows the number of measurements of B_{185} and (C) shows the fitted value of $B_{185\text{-mode}}$ in each ∼875 km^2 sector (0.5° × 0.5° at the equator).

4.2. Morphological comparison to global magnetometer maps

The first test of the ER crustal magnetic map (Fig. 1C) is that it must be morphologically consistent with the unambiguously crustal features of the global vector maps of total (i.e. crustal + external) magnetic field at the mapping orbit altitude of 370–430 km on the nightside (Acuña et al., 2001). We choose to compare to the radial component of the field (Fig. 1A) because it is less contaminated by external fields than the tangential components (Acuña et al., 1999; Connerney et al., 1999) and because the ER method only works when the total magnetic field is reasonably radial, allowing loss cones to form. Crustal magnetic fields are expected to vary on length scales comparable to and somewhat longer than the ∼400 km altitude of observation (Blakely, 1995) and this is clearly the case for the strong crustal signatures. From this we can infer that features weaker than 8–10 nT (i.e. colors darker than light blue) cannot be due to crustal fields because they form irregularly shaped streaks 1500–3000 km in length, consistent with the expected wavelengths of external fields (Brain et al., 2003).

Figs. 1A and 1C are entirely consistent with each other: every crustal feature in the magnetometer map is reproduced

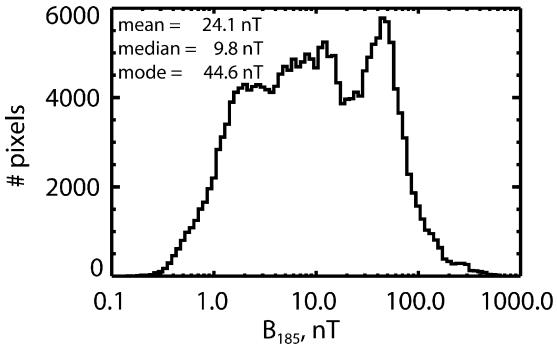

Fig. 2. Histogram of $B_{185\text{-mode}}$ for all sectors of the map shown in Fig. 1C. Values for the mean, median and mode of the distribution are inset.

in the ER map. Indeed there are many weaker sources visible in the latter that are below the detectability threshold for crustal fields in the former. This is to be expected, as the ER method measures the crustal magnetic field at approximately half the distance from the magnetized crust, resulting in 4–8 times greater sensitivity to crustal fields, depending on the exponent $p(2.0–3.0)$ by which the crustal field decreases with altitude. Also, as shown by Fig. 11 of Appendix B, its sensitivity is greater for weak crustal fields than for strong fields, while the opposite is true for the magnetometer map.

4.3. Global distribution of crustal fields

The global distribution of B_{185} is shown in histogram format in Fig. 2. We see that it is quite plateaued with 92% of the sectors in the wide range 0.4–100 nT. It is a wide distribution, implying that the magnetic moment of the crustal sources (and hence the magnetization) must be highly inhomogeneous with no particular strength dominating on a global scale.

4.4. Map accuracy and sensitivity

We now examine the accuracy of the map and its sensitivity threshold to crustal magnetic fields using the following measures: (1) the loss cone shape fitting errors in B_{185} and (2) the variation of $B_{185\text{-mode}}$ in each traced, smoothed geographical sector across 2 equivalent subsets of the full data set. Both are shown in Fig. 3, binned as a function of B_{185}. In weak field regions, there is a lower limit of ∼4 nT for individual errors, controlled by the instrumental flux uncertainties in the pitch angle bins (i.e. the left side of the 1-σ error ellipsoid, like that in Fig. 12, is usually near 4 nT even when the best fit is near zero). This error increases slowly to ∼30 nT at 300 nT, or about 10%.

However, a better way to measure the uncertainty in a geographical sector, or more practically, to determine whether or not a particular magnetic feature has a crustal or external origin, is to see how $B_{185\text{-mode}}$ varies from one subset of the data set to another seasonally equivalent subset (i.e. the same fraction of a martian year, to avoid seasonal biases). Thus, we define our sector error to be half the difference between values of $B_{185\text{-mode}}$ from each equivalent 1.75 martian year subset

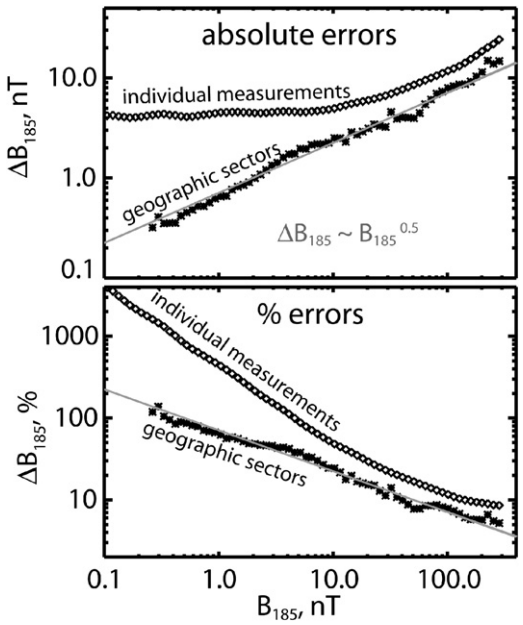

Fig. 3. Average absolute (top panel) and percentage (bottom panel) error in B_{185} as a function of B_{185} in 70 logarithmically spaced bins. Diamonds represent the loss cone fitting error for each individual measurement and asterisks represent half the difference between values of $B_{185\text{-mode}}$ in each 'smoothed' geographical sector from two seasonally equivalent 1.75 martian year intervals of the mapping phase of the mission. The red line is the best fit to a square root function.

of the mapping phase of the MGS mission, starting from the same point in the martian southern winter (solar longitude or 'L_S' = 132°), spanning the intervals: 1999/05/01–2002/08/15, 2003/02/03–2006/05/20.

As shown in Fig. 3, this sector error is approximately proportional to the square root of $B_{185\text{-mode}}$ and considerably lower than the individual errors because each sector typically contains hundreds of measurements. This is especially true for lower values of B_{185} due to the aforementioned greater sensitivity of the loss cone shape to weak crustal fields than strong fields. Nonetheless, the percentage errors are considerably larger for weaker fields due to small, unpredictable gradients in the external field reinforcing or inhibiting magnetic reflection from crustal fields, depending on their relative orientation. For example, an external magnetic gradient as low as 10 fT/m (0.01 nT/km) can obscure a crustal magnetic field of 2 nT at 185 km. Indeed, some of the features we see on the map weaker than ∼4 nT are likely the result of these external gradients, not crustal magnetization, and are inconsistent across different subsets of the data. Thus we consider 4 nT as a global sensitivity threshold for detection of crustal magnetic fields and use it as a lower limit on the color scale when plotting the global map. It can be thought of as a global upper bound for the crustal field magnitude in magnetically weak regions of Mars, though there are some large regions, such as the Utopia basin and the very great majority of the Tharsis province, where B_{185} is everywhere <2 nT.

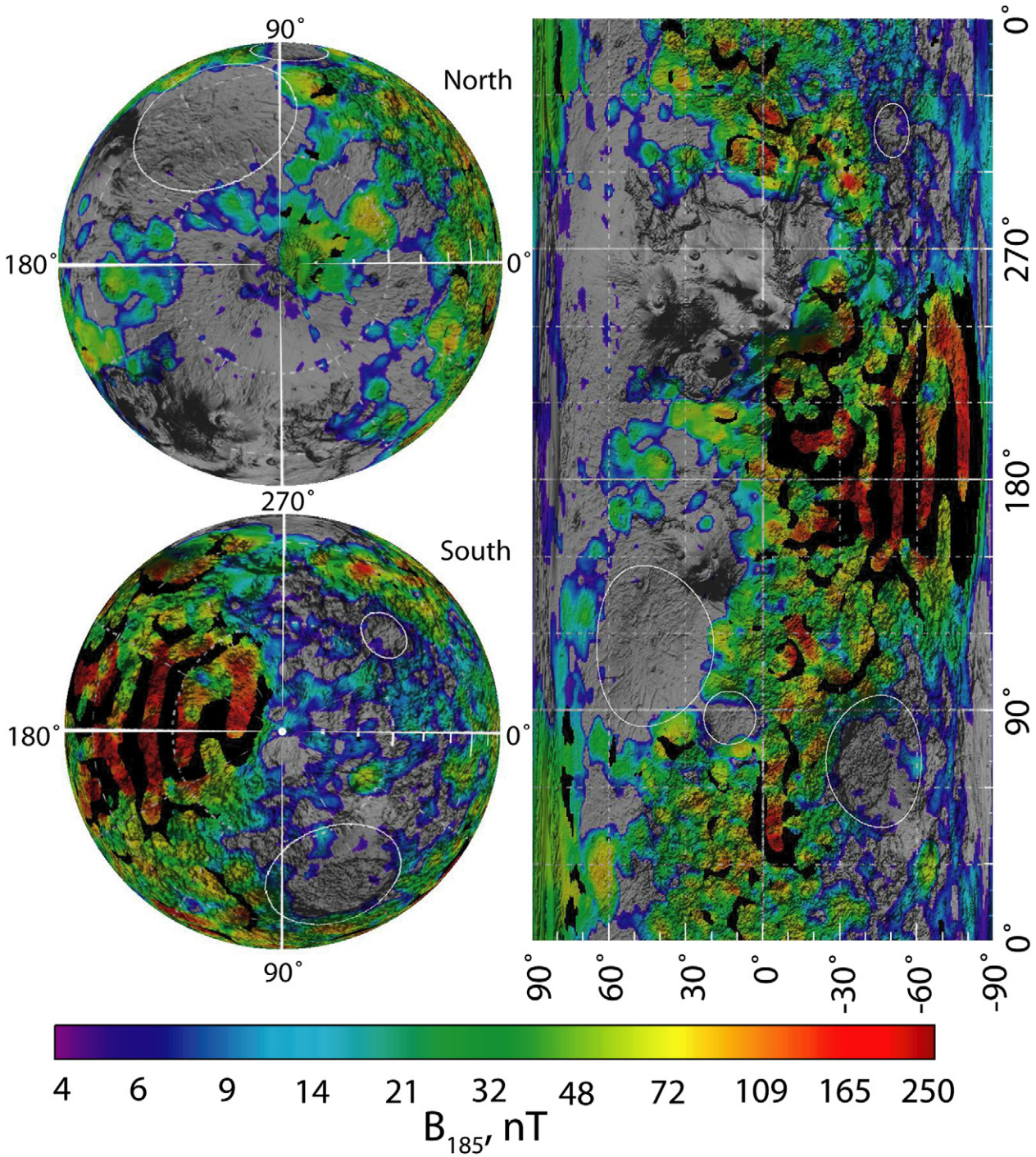

Fig. 4. 'Smoothed' ER magnetic map of Mars in polar projections (left) and cylindrical projection (right). The logarithmic color scale represents the crustal magnetic field magnitude 185 km above the martian datum and is overlaid on shaded MOLA topography (Smith et al., 2001). The lower limit of the color scale is the threshold for unambiguously crustal features while the scale saturates at its upper end. Black represents sectors with fewer than 10 measurements within a 100 km radius. The four largest visible impact basins (from left to right: Hellas, Isidis, Utopia, and Argyre) are shown with white circles.

5. Finished ER global map of martian crustal fields

We are now in a position to present the ER global map of crustal magnetic field magnitude at a common altitude of 185 km above the areoid (defined in Section 2). Fig. 4 shows this map, in both cylindrical and polar projections, fully filtered, corrected and smoothed (as defined in preceding sections), and overlaid upon shaded 0.25° × 0.25° topography from the Mars Orbiter Laser Altimeter (MOLA) experiment (Smith et al., 2001). Its spatial resolution is ∼200 km, which can be deduced from the altitude of observation (Blakely, 1995), although this is effectively worsened somewhat by the location errors described in Appendix D. The lower limit of the color scale is the sensitivity threshold for detecting unambiguously crustal

fields: 4 nT. The upper limit of 250 nT, though it causes saturation in places, encompasses most of the dynamic range of the map while still clearly displaying variations in crustal field strength below ∼40 nT at 185 km (i.e. 5–10 nT at 400 km) an important range at or below the sensitivity of the global vector magnetic map (Acuña et al., 2001). Black regions indicate pixels with fewer than 10 measurements within a 100 km radius and so represent typically closed crustal magnetic field lines (i.e. connected to the crust at both ends).

Since a global electron reflectometry map of martian crustal magnetic fields has already been published by Mitchell et al. (2007), it is important to point out that the purpose of this article is not to elucidate the method by which the previous map was constructed and present the same map. The 11 separate improvements over this earlier work (listed in Appendix G) result in a map that is not dramatically different in its global character from that presented in Mitchell et al. (2007), underlining the robustness of the general technique. However, the weaker field values and crustal field detection threshold are significantly lower due to the more appropriate distribution fitting. In addition, the relative magnetic field magnitudes in some adjacent regions, as well as small-scale morphology, are different in this new map.

6. Comparison with low altitude MAG data

A comparison between the ER map of B_{185} and in situ magnetometer measurements made at 185 km during the aerobraking and science phasing orbits of MGS would seem like an excellent test of the ER method. Such a comparison is shown in Fig. 5. However, confusing matters is the fact that B_{185} is a measure of crustal-only fields taken in the martian shadow, while the vast majority of low-altitude MAG data taken during these mission phases is taken on the martian dayside and consists of both crustal and external fields. The data we compare directly with B_{185} is represented in the low-altitude MAG data cube as an average of all measurements taken between 180 km and 190 km in each 1° by 1° pixel. At these altitudes, MGS is well above the ionospheric peak and the piled-up interplanetary magnetic field varies between 15–30 nT at the

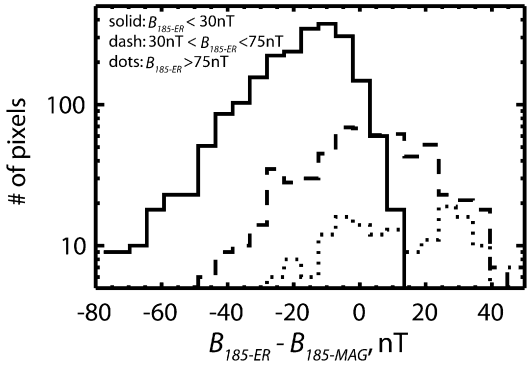

Fig. 5. Histogram of differences between the crustal field magnitude at 185 km as determined by electron reflectometry (i.e. B_{185}) and the total field magnitude at 185 km as measured by MAG, split up into three intervals of B_{185} values. There are 3270 1° by 1° pixels (∼1.5% of the planet) with enough MAG measurements between 180 and 190 km to make this comparison with B_{185}.

terminator to ∼50 nT at the sub-solar point (Acuña et al., 2001; Brain et al., 2003). This piled-up field, produced by ionospheric currents, should add approximately vectorally to the crustal fields, reinforcing or canceling them. This is indeed what we see in Fig. 5. In weak crustal field regions where the ER method determines the crustal fields to be <30 nT, most of the field magnitude measured by MAG on the dayside in situ is external (i.e. ionospheric) and so has a median value of ∼15 nT higher than that the crustal-only fields measured by ER on the nightside. On the other hand, for stronger crustal fields, between 30 and 75 nT, the external field's magnitude is of the same order as the crustal field and so is as likely to partially cancel it as to reinforce it, resulting in a distribution of differences approximately centered on zero (median value of 1.3 nT). For values stronger than 75 nT, ER measurements are slightly higher than MAG measurements (median difference of 6 nT), but statistics are poor and since such fields are easily observable with the 400 km MAG data, we shall not be concerned with these small differences. So although a side-by-side comparison between low-altitude, dayside MAG measurements of the total magnetic field near 185 km and crustal-only values of B_{185} is not as revealing as we would wish, the two data sets are certainly consistent with each other if we allow reasonable assumptions for the dayside external magnetic fields.

7. Use of map for geophysical investigations: Volcanoes and impact craters

This article is primarily concerned with the construction of the ER map, comprehensive analysis of which is beyond our present scope. However it is important to highlight areas of study opened up by the greater spatial resolution (factor of 2) and sensitivity (factor of 4–8) of the ER map compared to previously published MAG maps (Acuña et al., 2001).

Volcanoes and impact craters can be thought of as 'magnetic markers' in that their formation (and, for volcanoes, continuing activity) completely or partially "resets" the geological clock, in terms of surface age and crustal magnetization. In the case of volcanoes, lava flows (if deep enough) reset surface ages and magmatism causes thermal demagnetization of crust. In the case of impacts, excavation of magnetized material, along with shock and thermal effects, reduces average crustal magnetization during the impact. The ambient magnetic field present at these "reset" events is recorded in the consequent re-magnetization by thermoremanent (TRM) or shock-remanent (SRM) processes, which we may then observe as patterns of crustal magnetic field (keeping in mind the intrinsically nonunique relationship between magnetization and magnetic field). Of course, subsequent shock, chemical, or thermal events will alter these patterns so one must interpret them carefully, paying close attention to geological context. The increased resolution (∼200 km) of the ER map compared to the MAG map (∼400 km) allows us to study the magnetic signatures of a substantially larger number of impact craters and volcanoes than was previously possible (e.g. Hood et al., 2003; Nimmo and Gilmore, 2001; Johnson and Phillips, 2005). It is this framework in which we present two case studies. The first

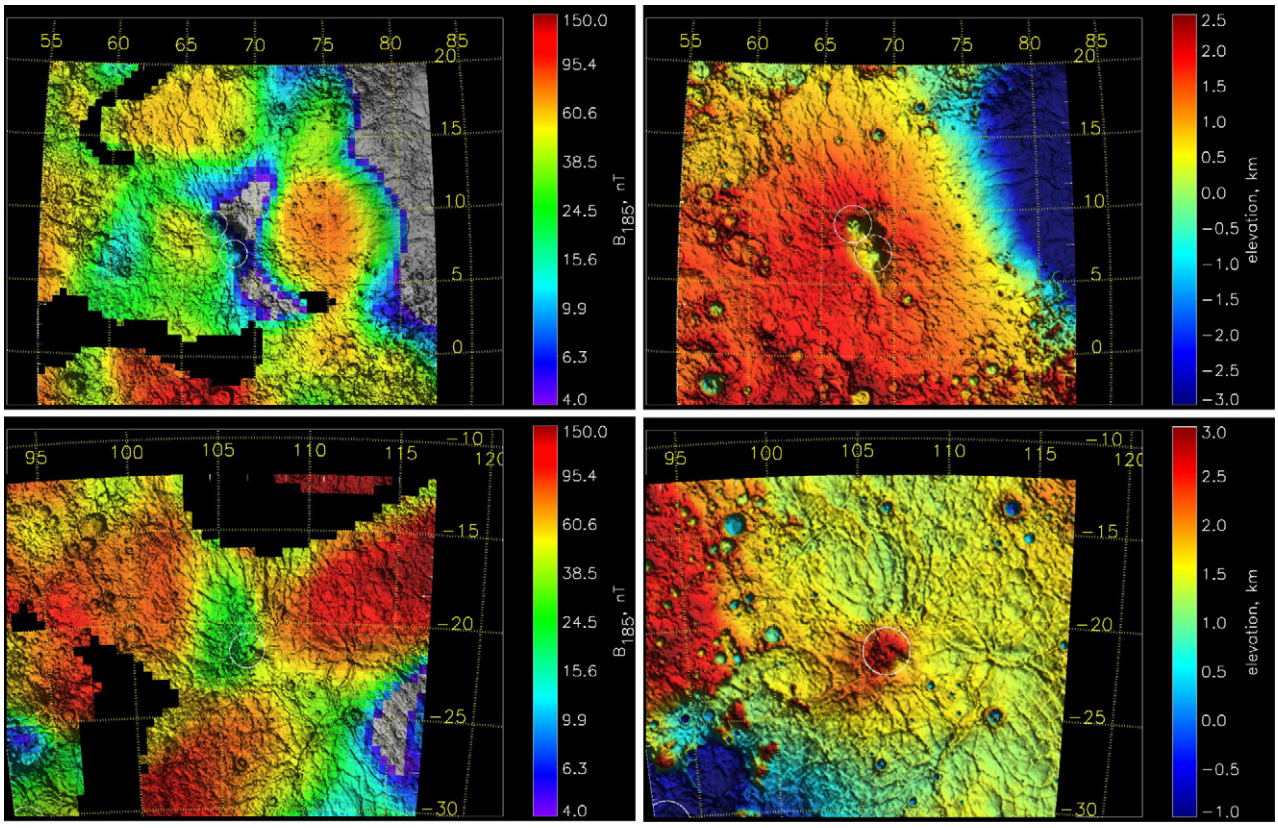

Fig. 6. ER magnetic (left) and MOLA topographic (right) maps of the Syrtis major volcanic province (top) and the Tyrrhena Patera volcano (bottom). Calderas are shown with small white circles, with Nili Patera located ∼200 km NNW of Meroe Patera in the top panels.

compares the magmatic and magnetic history of two volcanoes in the southern highlands, while the second uses the magnetic signatures of two large impact basins to bracket the death of Mars's early dynamo.

8. Magmatic demagnetization: Syrtis Major vs Tyrrhena Patera

On Earth, the magnetic signature of volcanoes is distinctive enough to identify buried volcanoes (e.g. Behrendt et al., 1998) and to study their history and constrain the volume of subsurface magma (e.g. Maia et al., 2005). An important distinction for martian volcanoes is that volcanoes on Earth always form (and currently exist) in the presence of a core-generated magnetic field, and hence all magmatic products will acquire a thermoremanent magnetization as they cool, in addition to possessing induced magnetization. In contrast, the martian dynamo likely ceased more than 4 Ga (Acuña et al., 1999; Frey, 2006), at or before the earliest datable volcanic activity of any large martian volcano (e.g. Plescia, 2004). Some volcanoes may have been active earlier and in the presence of the global dynamo magnetic field, e.g. Hadriaca Patera (Lillis et al., 2006) or Apollinaris Patera (Whaler and Purucker, 2005), but most if not all have experienced significant magmatism in the absence of such a field. Therefore, the magnetic signature of martian volcanoes should thermal be dominated by demagnetization, and magnetic anomalies due to remagnetization may often be absent. The degree and extent of demagnetization, as inferred from the magnetic field, can therefore be used as a rough proxy for the location and volume of magma intruded beneath a martian volcanic edifice, and thus offers insights that may be complementary to those provided by gravity, topography, and surface imaging. We caution, however, that B_{185} is only a proxy for crustal magnetization, given the inherent nonuniqueness of the inversion problem, and only at wavelengths of $\geqslant$200 km (Blakely, 1995). Nevetheless, because we expect the magnetic signature to be dominated by demagnetization, it is most straightforward to interpret the reduction in magnetic field amplitude seen above volcanoes (e.g. Whaler and Purucker, 2005; Johnson and Phillips, 2005) to indicate changes in the thickness of the magnetized crust.

Fig. 6 shows the ER magnetic signatures and MOLA topography (Smith et al., 2001) of the Syrtis Major volcanic complex (∼7° N, 67° E) and the Tyrrhena Patera volcano (∼21° S, 107° E). Their edifice sizes are 1000 × 1400 km and 215 × 350 km respectively (Plescia, 2004). The crustal magnetic field surrounding both volcanoes is highly variable, ranging from <4 nT to >100 nT at 185 km, indicating strong gradients in crustal magnetization, with substantial regions (i.e. black areas) inaccessible due to closed crustal field lines. Tyrrhena shows weak crustal magnetic field (∼25 nT) over the caldera and a region to its north and west, compared to surrounding regions, while for Syrtis we notice an hourglass-shaped region ∼550 km × 250 km and slightly offset to the east from the Nili and Meroe Caldera complex, where the crustal magnetic field is below 4 nT. For both volcanoes, this is consistent with thermal

demagnetization of crust by magmatic intrusion in these weak crustal field regions. If this is the case, the degree of demagnetization is far more complete for Syrtis than it is for Tyrrhena, at least locally. These weak field regions need not necessarily be centered on the calderas due to location errors in the data of typically 50–100 km and the fact that the subsurface magma distribution need not be symmetric about them. As long as they can reasonably be argued to coincide with the edifices, we may confidently associate them with the volcanoes.

Because the depth of magnetization extends many km below the surface (Acuña et al., 1999), the demagnetization inferred from the absent or nearly absent magnetic field must be dominated by intruded magma bodies such as sills, dikes and magma chambers. To assess the volume of such intrusions needed to demagnetize the crust, we performed a set of simulations in which sills were randomly intruded within a crust and determined the relationship between the volume of intrusion and the fraction of crust heated above the Curie temperature of potential magnetic carriers (assumed to be 320 °C for pyrrhotite, 580 °C for magnetite and 670 °C for hematite). Briefly, these simulations solve the 1-dimensional heat conduction problem in which basaltic sills with a 100 m thickness (Wilson and Mouginis-Mark, 2003; Ernst et al., 2001) and temperature of 1140 °C are randomly intruded at depths between 2 and 15 km over a 100 Ma time period. The 1-dimensional approximation of the model is equivalent to assuming that the sills extend for horizontal distances that are large compared to their thickness. We assume a background heat flow of 60 mW/m^2, appropriate for early martian history (Williams and Nimmo, 2004) and consistent with the thickness of the elastic lithosphere when Syrtis formed (Kiefer, 2004). With a thermal conductivity of 1.6 $W\,m^{-1}\,K^{-1}$ (Ingebritsen et al., 1994) the Curie temperature of magnetite (580 °C) is reached at a depth of 15.5 km, which is why we focus of intrusions within the upper 15 km. Lillis et al. (2006) showed that the period over which intrusions accumulate has little effect on implied demagnetization provided it is more than a few Ma. Ogawa and Manga (2007) showed that hydrothermal circulation will similarly have little effect on thermal demagnetization except for the case of pyrrhotite, and in this case, only if crustal permeabilities are greater than 10^{-15} m^2.

Fig. 7 shows that intrusion amounting to a couple of km will thermally demagnetize most of the magnetized crust if the dominant carrier is pyrrhotite. On the other hand, if the dominant magnetic carrier is magnetite or hematite, the volume of crust that is demagnetized is similar to the volume of magma intruded into the formerly magnetized crust. In this case, more than 10 km of post-dynamo lavas and intruded magmas must make up the upper 15 km of crust. One of the few other observational constraints on the amount of intruded magma is gravity. Kiefer (2004) used gravity and topography measurements to infer the presence of what he called magma chambers with minimum thicknesses of between 3–4 km. Fig. 7 shows that these minimum thicknesses, if this was the only intruded magma, would be unable to completely demagnetize a crust in which the dominant carrier was magnetite or hematite.

The volume of accumulated surface lavas and erupted materials at both Tyrrhena and Syrtis are similar. Hiesinger and Head (2004) estimate effusively emplaced lava thicknesses of 0.5–1.0 km over the Syrtis province, totaling 1.6–2.5 × 10^5 km^3, deposited in the late Noachian/early Hesperian. Gregg and Farley (2006) estimate that mafic pyroclastic deposits of 1.8–2.2 × 10^5 km^3 make up the bulk of Tyrrhena's volcanic edifice, similar in volume to Syrtis. The character of Tyrrhena's volcanism transitioned from explosive to effusive in the early Hesperian era (Crown and Greeley, 1993), producing a lava flow field of ~200,000 km^2 with thicknesses of 50–90 m (Meyer and Gregg, 2001), totaling 1.0–1.8 × 10^4 km^3. Assuming the original magnetic carriers and properties of the crust were the same at both volcanoes, the greater demagnetization at Syrtis must imply a greater ratio of intrusive to extrusive magmatism, a ratio hereafter referred to as the I:E ratio.

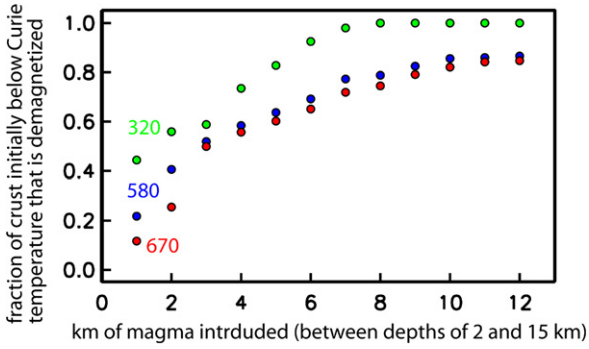

Fig. 7. Thermal demagnetization by magmatic intrusion. The fraction of crust shallower than the Curie isotherm that is raised above the Curie temperatures of pyrrhotite (green), magnetite (blue) and hematite (red) is plotted as a function of the thickness of magma randomly intruded in 100 m-thick sills over 100 million years. See text for details of calculation. (For interpretation of the references to color in this figure legend, the reader is referred to the web version of this article.)

The I:E ratio is unknown for Mars. Greeley and Schneid (1991) assumed a range from 5:1 to 12:1, similar to the widely adopted value for Earth of 10:1 (e.g. Crisp, 1984). The I:E ratio, however, is not easily determined and hence not well constrained on Earth; where estimates are available, it is highly variable, ranging from ~1:1 in Hawaii (White et al., 2006) to >100:1 at the Coso Volcanic Field (Bacon, 1982). Even in a given geological setting, it can be highly variable. For example, in the Cascade range, USA, it varies by as much as a factor of 10 (Blackwell et al., 1990; Sherrod and Smith, 1990). White et al. (2006) provide a recent review and note that their compilation 'fails to show any systematic variations with eruptive style, volcanic setting, or volume.'

Given the variability of I:E ratios on Earth, it is difficult to draw robust conclusions about the apparent difference in I:E ratio between Tyrrhena and Syrtis. Nevertheless, we offer three explanations. First, in systems that erupt more evolved and differentiated magmas, the I:E ratio should increase (e.g. Wadge, 1982). Bandfield (2006) used THEMIS data to infer the presence of differentiated (granitoid) magmas at Syrtis, though it is not known whether similar magmas may exist at Tyrrhena. Second, in regions with active extension, the expansion of the crust makes room for magma allowing the possibility of greater I:E ratio. The location of Syrtis next to the Isidis basin provides gravitational potential that will promote and permit extension

(Hiesinger and Head, 2004, Fig. 22). Observational support for extension increasing the I:E ratio is provided by basaltic volcanism on Earth's seafloor. The I:E ratio at Hawaii is ∼1:1, but where there is active extension, such as mid ocean ridges and Iceland, it is closer to 5:1 (White et al., 2006). Third, and somewhat speculatively, the pyroclastic shield-building deposits at Tyrrhena imply explosive volcanism, which may suggest more buoyant magmas and hence lower I:E ratios, compared with the effusively emplaced lavas at Syrtis. It should be pointed out that we only considered thermal demagnetization in our discussion. Though no visible evidence exists for long-lived hydrothermal systems, chemical demagnetization from such systems should be recognized as a possible alternative explanation.

Regardless of the reason for the different magnetic signatures of Syrtis and Tyrrhena, the ER magnetic map illustrates that its spatial resolution is sufficient to use magnetic fields to probe martian volcanoes and their history. Moreover, if the difference in magnetic signatures we see are in fact caused by different I:E ratios as suggested here, Mars may offer a unique opportunity to measure I:E ratio, a quantity that is difficult to measure on Earth. Despite being poorly determined, the I:E ratio is of critical importance for establishing the thermal history of the martian mantle (e.g. O'Neill et al., 2007), and to probe the structural and petrotectonic evolution of the martian crust.

9. Hellas versus Ladon basins: Bracketing the end of the martian dynamo

It is certain that Mars possessed a global magnetohydrodynamic dynamo at some point in the past (Acuña et al., 1999; Connerney et al., 1999). From the lack of detectable crustal fields in the largest visible basins (highlighted in Fig. 4), it has been concluded that the dynamo had stopped operating by the time of the first of these visible impacts, early in the Noachian era, ∼4.1 Ga ago and still was not operating by the last of them, the Isidis impact, ∼3.9 Ga ago (Acuña et al., 2001; Frey, 2006). The observed lack of magnetized crust unambiguously younger than ∼3.9 Ga suggests there were no subsequent episodes of dynamo activity. In order to more precisely bracket the time interval during which the global magnetic field decreased from substantial to very weak or nonexistent, we perform a side-by-side comparison of two impact basins who fall temporally on opposite sides of the cessation of the dynamo, as determined by their relatively clear magnetic signatures.

9.1. ER magnetic signatures of the basins

The Ladon basin (330° E, 17° S) is an old, degraded, multi-ringed basin whose outer ring is ∼950 km in diameter. Fig. 8 (top panels) shows both ER magnetic and MOLA topographic maps of the Ladon region. Ladon has been partially overlaid by three large basins including the Holden basin to the SSW and by the Margaritifer Chaos basin to the NE.

Its magnetic signature consists of an approximately annular region of weak or nonexistent crustal fields, following the contours of the outer ring, surrounding a substantial local magnetic maximum ∼200 km off-center to the southeast. We interpret this as shock demagnetization of an area approximately equal to that inside the outer ring, followed by subsequent re-magnetization of part of the inside of the crater. The process by which this re-magnetization occurred is not important for the purposes of this article. We wish only to emphasize that such remagnetization requires the presence of a global magnetizing field existing at some point in time after the impact occurred. However, given that the signature is interesting and unique on the planet, let us qualitatively consider some possible explanations for the magnetic maximum inside the crater being offset from its center.

The lack of symmetry is puzzling. Calculations of the magnetic field, at 185 km altitude, of a crater-centered uniformly magnetized disc of the appropriate dimensions for Ladon show that the magnetic maximum can be at most ∼100 km off-center due simply to direction of magnetization. The remaining offset could possibly be due to tracing errors of 50–100 km in the ER map (see Appendix D), an unlikely explanation because these two offsets would need to be in almost exactly the same direction, though we cannot rule it out. Therefore, this is not easily explained as a simple, unmodified, magnetized, solidified melt pool. If such a pool remained after the impact, its magnetization could have been altered by subsequent small impacts or by asymmetrical aqueous mineral alteration in a post-impact hydrothermal system that may have remained for several million years or longer (Daubar and Kring, 2001; Abramov and Kring, 2004). Alternatively, the off-center magnetic maximum could be explained by post-impact magmatic intrusions in the northwestern part of the crater center, although no obvious large-scale topographic evidence of this is visible. Regardless, we may confidently argue that the impact caused shock demagnetization as far as the outer basin ring, on the evidence that (1) this ring forms the outer boundary (around much of the crater's circumference) of the annular region of extremely weak magnetic field surrounding the off-center positive anomaly and (2) the comparably sized Isidis basin (∼1200 km in diameter, highlighted in Fig. 4) displays shock demagnetization approximately as far its main rim. If, as seems very likely, such shock demagnetization occurred, then it is almost indisputable that a significant global magnetizing field was present at some point after the impact.

The Hellas basin is the largest visible impact basin on Mars at ∼ 2000 km in diameter and was formed near the end of the Late Heavy Bombardment of asteroids and comets ∼4.1 Ga ago (Frey, 2006). It is devoid of all but the weakest crustal magnetic fields, as shown in Fig. 8, and is therefore widely regarded to have formed in the absence of any substantial global magnetic field (e.g. Acuña et al., 1999), though it should be pointed out that this interpretation is not universally accepted (Carporzen et al., 2005; Solomon et al., 2005). As discussed in the introduction, it is probable that the dynamo never started again after the Hellas impact.

It should be acknowledged that the demagnetization of both these basins was investigated by Shahnas and Arkani-Hamed (2007), who also concluded that Hellas was demagnetized and Ladon likely magnetized.

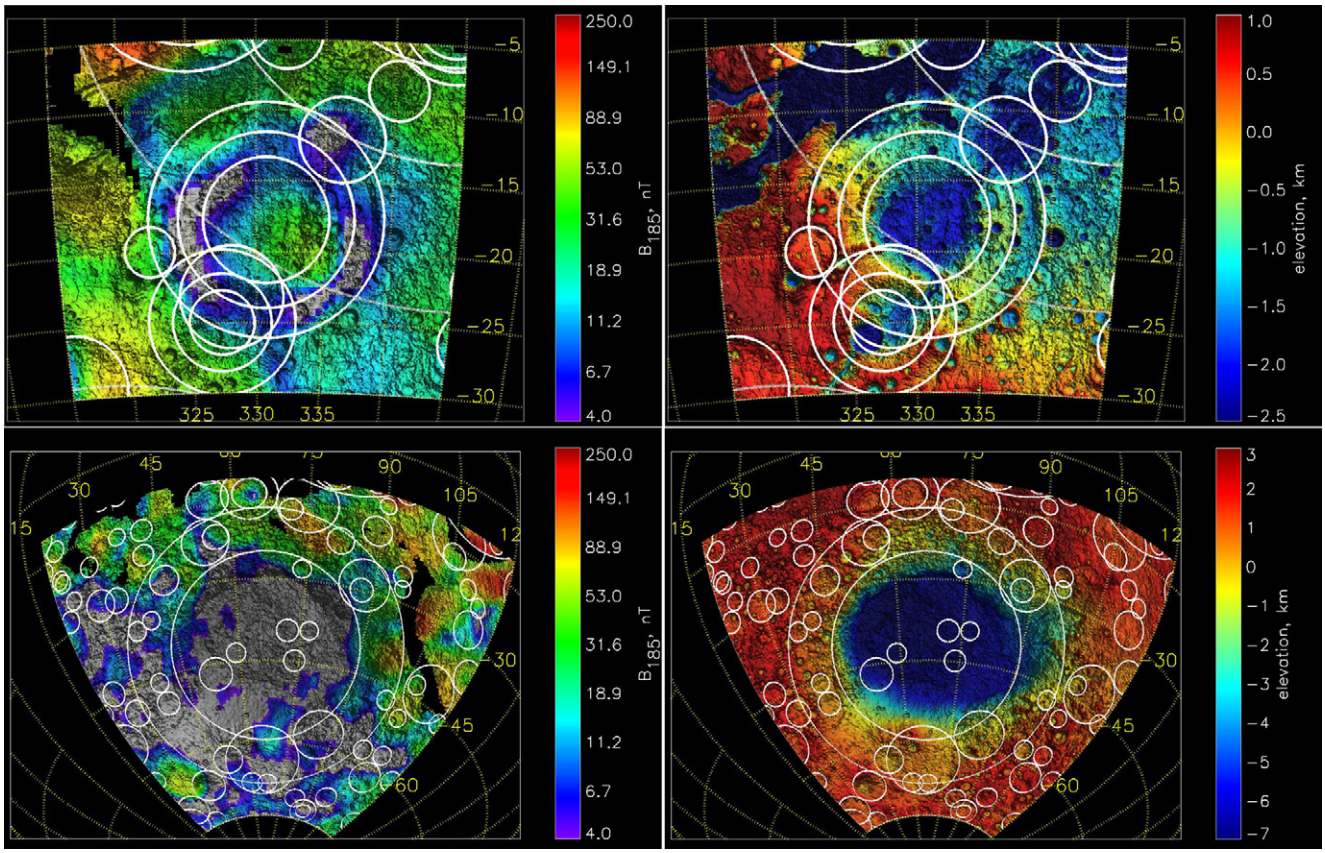

Fig. 8. ER magnetic (left) and MOLA topographic (right) maps of the Holden–Ladon basin complex (top) and the Hellas basin (bottom). White circles represent all visible and buried craters larger than 200 km. In the top panels, Ladon is the large central basin, while Holden is the substantial multi-ringed crater to its southwest and Margaritifer Chaos lies immediately to its northeast.

9.2. *Crater retention ages (CRAs) of the basins*

We attempt to determine the ages of the Hellas and Ladon basins relative to each other and other stratigraphic units on Mars by considering the cumulative density of overlaid craters larger than a range of sizes. Using quasi-circular depressions (QCDs) identified in MOLA data as proxies for buried craters (Frey, 2006), we carried out a comparison of total crater population (visible + buried) for the Holden–Ladon region and Hellas. Maps of the areas used and the resulting cumulative size-frequency curves, are shown in Fig. 9. In the case of Ladon, the counting area encompasses the entire basin as well as the Holden, Margaritifer Chaos and other basins which clearly overprint the rings of the Ladon basin. In the case of Hellas, the northern rim is chosen instead of the basin floor to reduce the effects of significant burial of smaller craters by fluvial and aeolian deposition over time. Insofar as possible, we confined the Hellas counts to the folded, uplifted portions of the northern rim of the basin (Leonard and Tanaka, 2001) to ensure we were counting only post-Hellas, superimposed impact craters. Over the 30–100 km diameter range the two curves are identical within their errors. Because these curves are so similar to cumulative size-frequency curves for other very old areas of Mars, they may represent actual saturation over this diameter range. At $D > 100$ km, Holden–Ladon basins continue to follow a -2 power law trend, but the Hellas points plot lower than the trend. While this could be due to poor statistics in the larger size range for Hellas, both counting areas are the same ($\sim$1.2 M km^2). Thus we suggest this may represent a real age difference: if the -2 power law trend indicates saturation, Ladon has undergone (near) saturation to larger diameter craters than has Hellas because it is older than Hellas.

We obtain a value for the N(100) CRA (i.e. the number of overlaid craters greater than 100 km in diameter per million square kilometers) for Hellas of 9.9 which, following the -2 power law, is consistent within errors with the N(200) CRA of 2.7 calculated by Frey (2006) using only craters >200 km in diameter over the entire Hellas basin (these craters are less susceptible to erosion and burial). For Ladon, we obtain N(100) = 13.8. When these are converted to a minimum absolute model age using Frey's (2006) modification of the cratering chronology of Hartmann and Neukum (2001), we obtain $>4.07 \pm 0.05$ Ga and $>4.15 \pm 0.05$ Ga for Hellas and Ladon respectively, thereby indicating that the martian dynamo ceased or weakened significantly during this time period. Due to the lack of radioisotope dating of martian surfaces (i.e. to calibrate the cratering record), absolute ages calculated in this fashion may have large systematic uncertainties (up to a factor of two) but relative ages of surfaces are thought to be reliable (Hartmann and Neukum, 2001).

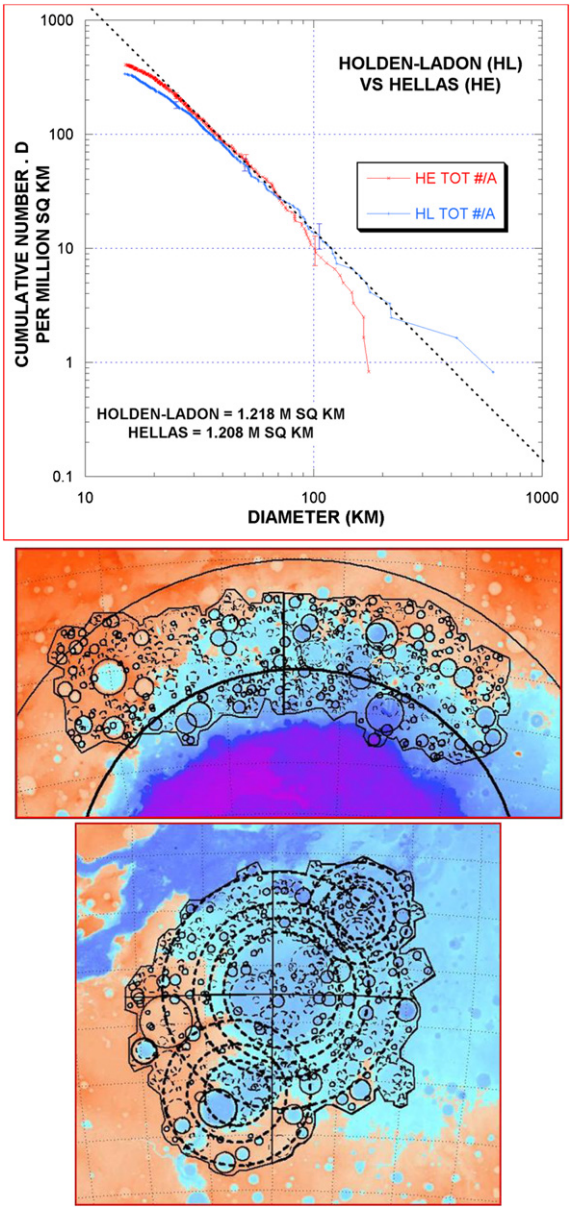

Fig. 9. A comparison of QCD cumulative size-frequency curves for Holden–Ladon (blue) and Hellas (red) and maps of the areas and individual craters used to produce those curves. Craters visible in photographs are represented by solid circles, while craters only identifiable in MOLA topography ('buried' craters) are shown by dotted circles. (For interpretation of the references to color in this figure legend, the reader is referred to the web version of this article.)

10. Concluding remarks

To summarize, in this article we have:

1. Used a kinetic model of electron loss cone formation that predicts pitch angle distributions given profiles of the magnetic field magnitude and neutral density along the field line on which the electrons are traveling (Lillis et al., 2008a).
2. Chosen an appropriate parameterization for the magnetic profile (Section 2).
3. Defined the best mean atmospheric model to use as input (Appendix A).
4. Determined the mean altitude of greatest sensitivity for crustal fields: 185 km (Appendix B).
5. Showed that the magnetic profile needs just 1 free parameter to determine B_{185} (Appendix C).
6. Explained how we correct for the effects of electrostatic potentials (Appendix C).
7. Investigated location errors from straight field line tracing from ∼400 km down to 185 km (Appendix D).
8. Defined criteria for filtering out unusable data (Section 3).
9. Corrected, insofar as possible, for the masking of crustal fields by external fields (Appendix E).
10. Selected appropriate schemes for binning the data into geographic sectors (Section 3).
11. Applied a method for determining the most likely value of B_{185} in a given sector (Appendix F).
12. Highlighted global magnetic topology effects on the distribution of loss cones.
13. Compared the map directly to the global magnetometer-derived map at ∼400 km.
14. Showed that no single magnetic field strength dominates the global distribution.
15. Examined accuracy of the map and determined the average error in each sector.
16. Defined a global sensitivity threshold for unambiguous detection of crustal fields.

The result of these steps has been the presentation of a global map of crustal magnetic field magnitude 185 km above the martian areoid, with a crustal field detection threshold of 4 nT globally and as low as 2 nT locally, containing significant data gaps (∼9% of map) where crustal magnetic field lines are permanently closed. To illustrate applications of this map, we have presented two limited case studies examining magmatic processes at two highland volcanoes and the death of the global magnetic field >4 Gyr ago. We hope this map will be useful to the wider community when used in concert with topography and gravity data, orbital imagery and appropriate magnetic field-to-magnetization inversions, to investigate the correlations between magnetized crust and geological features in order to better understand the interconnected histories of hydrothermal processes, magmatism, volcanism, tectonism, impact cratering, and the ancient dynamo on Mars.

Acknowledgments

This work was supported by NASA grants JPL 1271721-05/06, JPL 08668-01/07 and by the NASA Mars Data Analysis Program Grant NNX07AN94G.

Appendix A. Assumed neutral atmosphere

We need to assume an atmospheric density profile if we are to use the loss cones to solve for the crustal magnetic field over the entire planet. Lillis et al. (2008b) used the same loss cone model explained in Lillis et al. (2008a) to derive nightside atmospheric neutral mass densities at 185 km over four martian

years in regions of the southern hemisphere where crustal magnetic field lines are open to the solar wind and where the crustal field is sufficiently strong as to dominate the induced magnetotail field. Here we use those results to construct a model atmospheric profile of number densities of each species (CO_2, O, O_2, N_2, CO and Ar) that is consistent with the overall mean neutral mass density profile compiled from all the loss cone-derived densities in Lillis et al. (2008b). This profile is not intended to accurately represent the true atmosphere at all times but to be a reference atmosphere that is as close to the mean as possible. Though this profile only represents densities measured in the Southern hemisphere (Lillis et al., 2008b), we expect annual mean density profiles to not be significantly different in the Northern hemisphere.

We use as a basis an MTGCM simulation of the thermospheric density profile at 2 a.m. at the equator, at Spring equinox under solar moderate EUV conditions (Bougher et al., 1999). The mean loss cone-derived mass density at 185 km (the altitude of greatest sensitivity, see Lillis et al., 2008b) is 6.6 g/km^3 or 1.1 times higher than this 'medium' simulated density. To avoid discontinuities and because our derived densities are less trustworthy as we get further from 185 km, we shall simply multiply the MTGCM-simulated number densities by this ratio at all altitudes, giving us a model reference atmosphere as shown in Fig. 10. The error bars were determined by modifying Eq. (25) of Lillis et al. (2008a), replacing the arbitrary variable y with mass density ρ, then calculating numerical partial derivatives of ρ with respect to scattering depth D for a typical strong crustal magnetic field profile and 100 sample atmospheres, logarithmically spaced from 0.01 to 100 times the mean reference model density profile at all altitudes. D can then be converted directly to reflection altitude because the magnetic profile is known.

We see that the errors increase above and below 185 km but stay comparable to the minimum error between ~175 and ~210 km. The errors increase dramatically below ~170 km and thus derived densities there are meaningless. Since these are theoretical uncertainties, their absolute values are unimportant

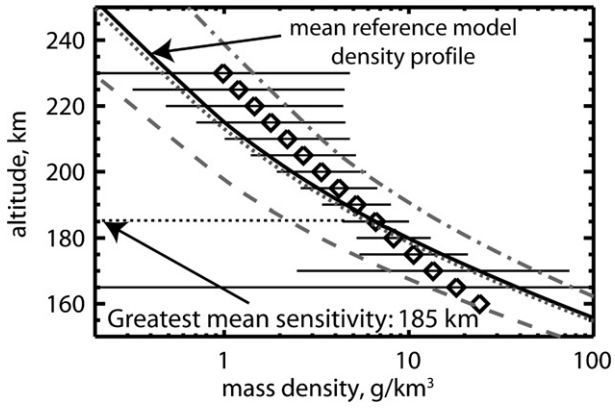

Fig. 10. Mean reference model density profile (solid black line) tied to derived density profile (black diamonds) at 185 km from Lillis et al. (2008b), plotted with MTGCM solar EUV minimum-aphelion (dashed), solar EUV moderate-equinox (dotted) and solar EUV maximum-perihelion (dash–dot) equatorial 2 a.m. simulated profiles.

but their relative variations with altitude show quite clearly that there is quite a sharp cut off at lower altitudes, below which the ER method has no sensitivity whatsoever.

When using measured loss cones to solve for magnetic parameters, we do not attempt to vary this assumed model mean reference atmosphere with the seasons because (1) we only have density data over ~1.5% of the planet and do not wish to extrapolate and (2) we sample the same geographic regions many times over more than 30,000 orbits and 3.75 martian years and therefore expect any atmosphere-induced seasonal variations in derived magnetic field values to average out. Interannual atmospheric variability (mentioned in Lillis et al., 2008b) is a very small effect, causing <1% differences in derived magnetic field magnitudes, and is ignored.

Appendix B. Altitude range of greatest sensitivity

To establish the altitude range of greatest sensitivity for the purposes of magnetic mapping, we utilize Eq. (25) of Lillis et al. (2008a) and in place of the arbitrary variable y we place B_c, the crustal magnetic field magnitude at a given altitude h, which we can express as:

$$B_c(h) = (B_{sc} - B_a)\left(\frac{z_{sc}}{z(h)}\right)^p. \tag{B.1}$$

This brings us to an expression for the fractional error in B_c:

$$\frac{\Delta B_c}{B_c} = \Delta P_{surv}\frac{\partial B_c}{\partial D}\frac{e^D}{B_c}. \tag{B.2}$$

By using our model reference mean neutral density profile and 600 different magnetic profiles (3 values of p, 200 values of B_c(185 km), $B_a = 12$ nT and the data set's median absolute magnetic elevation angle $\theta = 58.5°$), we can calculate 4 isomorphic two-dimensional (i.e. with respect to pitch angle, magnetic profile) arrays for 190 eV electrons: reflection altitude h, electron scattering depth D, crustal field magnitude at altitude h: $B_c(h)$, and the numerical partial derivative $\partial B_c/\partial D$. We can then combine them in Eq. (B.2) to determine how the fractional uncertainty in B_c changes with altitude and with crustal magnetic field strength, as shown in Fig. 11. The particular reference altitude for the crustal field, 185 km, is unimportant here: we simply want to show a range of different crustal field strengths. The first thing to notice is that the loss cones are much more sensitive to B_c when the crustal fields are weak, e.g. the fractional uncertainty is more than 20 times higher at 500 nT than at 5 nT, i.e. the loss cone will shift much further following an increase from 5 to 6 nT than from 500 to 600 nT. Secondly, we note that the altitude range of maximum sensitivity is quite narrow, less than 30 km and is weakly dependent on the strength of the crustal magnetic field. For B_c(185 km) > ~10 nT, the greatest sensitivity occurs at ~185 km. For weaker fields, this altitude is slightly higher but the error is still acceptably low at 185 km. Thirdly, the exponent chosen has a negligible effect on the altitudes of sensitivity or the relative errors and only a small effect on the absolute errors.

A magnetic map is much more useful for comparison between geographic areas if it is at a single common altitude than otherwise. The above evidence leads us to choose 185 km as the reference altitude for all crustal magnetic field strengths we shall derive from the loss cones. It is reassuring, though not surprising given the same mean atmospheric profile, that this is so close to 182 km, established by Lillis et al. (2008b) as the mean altitude of greatest sensitivity for ER mass density probing. It should be pointed out once again that 185 km is the altitude above the areoid, i.e. the equipotential surface given by the martian gravity model of Yuan et al. (2001) with a radius equal to the mean radius of the solid planet. This is because atmospheric density, which determines the absorption altitude of the incident electrons, responds to gravitational potential, not altitude above the solid crust.

It should also be pointed out that these are theoretical uncertainties, derived from our idealized model for the magnetic profile and, while very useful for defining relative errors with respect to altitude and crustal field strength, they ignore some of the real physical details present in the near-Mars plasma environment such as small external field gradients, currents and plasma waves as well as ER instrument errors in the positions of the flux bins in pitch angle space due to uncertainty in the magnetic field direction caused by spacecraft-generated fields. As such, these theoretical uncertainties form only part of the total uncertainties in the map of crustal magnetic fields. For example, ΔP_{surv} is typically $\sim$0.1 so according to Fig. 11, the theoretical uncertainty in a 10 nT crustal field is $0.1 \times \sim 0.3 \approx 3\%$ but the distribution of real measurements in a given geographical location is considerably wider than this and is dealt with in Section 4.

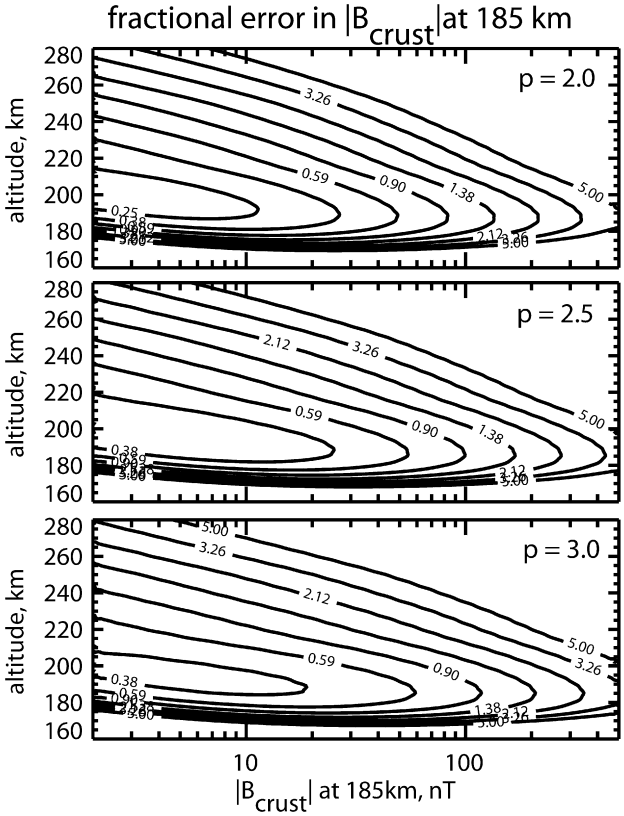

Fig. 11. Fractional uncertainty in B_c, the inferred crustal magnetic field magnitude for 190 eV electrons, is contour-plotted on a logarithmic scale, in units of ΔP_{surv}, as a function of altitude of electron reflection and crustal magnetic field strength (expressed as B_c at 185 km) for three different values of the crustal field exponent p. This leads us to choose 185 km as our reference altitude for crustal field strengths.

Appendix C. Fitting loss cones to derive crustal magnetic field strengths

Our next task is to fit our model to the measured loss cones to solve for the magnitude of the crustal-only magnetic field at 185 km or B_{185}, to which it shall now be referred. Specifically, we compare the loss cone in each instrument-measured pitch angle distribution to model loss cones (which are calculated by inserting values of B_a, p and the parallel electrostatic potential ΔV into Eq. (18) of Lillis et al., 2008a), then convolving from 50 model pitch angle bins to the 8 upward-traveling instrumental pitch angle bins (e.g. right half of Fig. 3a in Lillis et al., 2008a) that vary in width and position (Mitchell et al., 2001). We then calculate the goodness-of-fit χ^2, find its minimum and use Eq. (B.1) to determine B_{185}. The uncertainties are determined using the 1-σ error ellipsoid, i.e. the minimum and maximum values of B_{185} calculated from the range of the fitting variables for which χ^2 is less than its minimum plus unity. Only pitch angle bins with relative flux levels between 0.07 and 0.79 are used for fitting to avoid large errors, following the discussion in Section 7 of Lillis et al. (2008a).

The two-dimensional (i.e. B_a and p) χ^2 space and crustal field space associated with a typical loss cone fit, excluding parallel electric fields, are shown in Fig. 12. For the purposes of fitting, it is easier to deal with B_a/B_{sc}, the ratio of the ambient field to the spacecraft field because its value is always between 0 and 1. From an examination of the shape of the 1-σ error ellipsoid both in χ^2 space and crustal field space, it is clear that there is no unambiguously correct pair of values for B_a/B_{sc}, p within the physically reasonable range of values for p: the variables are highly correlated and we obtain the same value of B_{185} regardless of our position within the ellipsoid. This makes sense intuitively because we have already shown that the loss cones are mostly sensitive to crustal magnetic field magnitudes within a narrow range of altitudes (Fig. 11), i.e. only the crustal field in this narrow range is important, not the form of the magnetic profile at other altitudes. We may therefore safely pick a single fixed value of 2.5 for p and simply minimize χ^2 with respect to B_a/B_{sc} to solve for B_{185}. The fitting problem then reduces to one dimension, at least in terms of the magnetic profile, greatly reducing analysis time. Inclusion of parallel electrostatic potentials adds a new second dimension.

The presence of magnetic field-aligned or 'parallel' electric fields modifies the loss cones in an energy-dependent way while the effects of the magnetic profile are nearly energy-independent (Lillis et al., 2008a). Therefore, provided we have loss cone measurements in more than one energy channel, we can minimize χ^2 to solve simultaneously for crustal magnetic field and parallel electric field. First, consider the electrostatic potential $\Delta V(x)$ in Eq. (18) of Lillis et al. (2008a). Because the

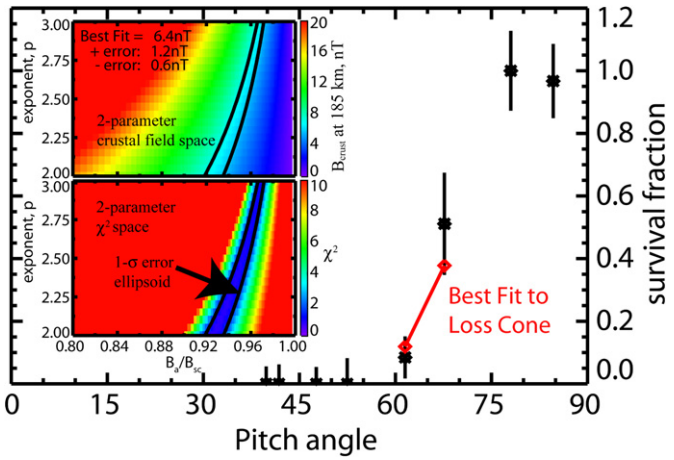

Fig. 12. Color plots of the 2-parameter χ^2 space (bottom) and associated crustal field space (top) corresponding to the loss cone measured at 2003-04-20/23:56:23, at 10.2° N, 82.0° E (West rim of Isidis basin). The 1-σ error ellipsoid is shown on both color plots by a pair of black curved lines, inside of which are the values of B_a/B_{sc} and p that represent the best fit.

loss cones are sensitive only to a narrow range of altitudes, we have no way to discern the altitude-dependent details of the potential (i.e. the 'electrostatic' profile) so we parameterize it by a constant parallel electric field E between the spacecraft and the electron absorption layer, which can be positive or negative and which represents the component of the true vector electric field which is parallel (or anti-parallel) to the magnetic field. It is worth emphasizing that this electric field is likely not the parallel component that would be measured at any given point between the spacecraft and the absorption region, but it is an average value over the total distance and is a convenient way of parameterizing the electrostatic potential difference along the field line. The perpendicular component of this field does not affect loss cone shapes directly; it can only cause plasma drifts which are much smaller than the typical length scale over which magnetic fields vary and thus may be ignored (Lillis et al., 2008a, 2008b). Modifying Eq. (18) of Lillis et al. (2008a), our model expression for pitch angle-dependent electron survival probability then becomes:

$$P_{\rm surv}(\alpha_0, E, U_0) = \exp\left[-2\sum_i \int_0^{x_r} \frac{\sigma_i(U_0 + eEx')n_i(x')\,{\rm d}x'}{\sqrt{1 - \frac{B(x')\sin^2\alpha_0}{B_0(1+\frac{eEx'}{U_0})}}}\right], \tag{C.1}$$

where e is the charge on an electron. This equation, combined with Eqs. (1) and (B.1), parameterizes our loss cone model in terms of B_{185} and E.

Though Eq. (C.1) is a single integral, calculating the entire two-dimensional χ^2 space for the $\sim 4 \times 10^6$ loss cones in the data set would be prohibitively time-consuming. We therefore employ an efficient gradient-search algorithm known as 'amoeba' (so-called because it 'slithers' around function space to find local minima; Press et al., 1992, p. 411) to quickly ($\sim$1 s) locate the χ^2 minimum and hence obtain best-fit values and estimated uncertainties for B_{185} and E. This article is primarily concerned with mapping crustal magnetic fields, so here we shall treat the parallel electric field results simply as a correction to improve the accuracy of the magnetic field results. Electric field analysis is left to future work.

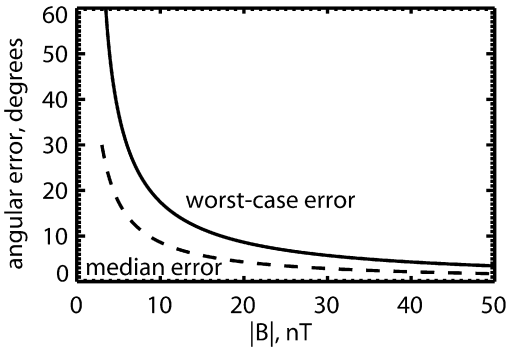

Fig. 13. Maximum error δ in measured magnetic field direction is plotted as a function of magnetic field magnitude $|\underline{B}|$.

Appendix D. Tracing magnetic field lines to 185 km

For every measurement of B_{185} we record the latitude and longitude of the spacecraft at $\sim$400 km altitude. However, since we are measuring crustal magnetic field magnitudes at 185 km, we must account for the shift in geographic location due to the magnetic field lines not being radial. We assume the field lines are straight between spacecraft altitudes (370 to 430 km) and 185 km and calculate at what latitude and longitude a straight line with the appropriate magnetic azimuth and elevation angle, intersecting the spacecraft, also intersects a sphere of radius $R_{\rm areoid} + 185$ km (the areoid is an equipotential surface with a radius equal to the mean radius of Mars, 3390 km). Errors in this tracing arise from 2 sources.

The first source is the uncertainty in the measured direction of the magnetic field at the spacecraft due to the presence of spacecraft-generated fields, as detected by differences between the two magnetometers mounted on the end of each solar panel (Acuña et al., 2001). We assume this difference to be a worst-case for the error in the ambient field and half this difference to be the median error, $B_{\rm err}$. These give a corresponding error, δ, in magnetic field direction:

$$\delta = \sin^{-1}\left(\frac{B_{\rm err}}{|\vec{B}|}\right). \tag{D.1}$$

3 nT is a good worst-case upper bound for $B_{\rm err}$ for most phases of the mission, resulting in a relationship between total magnetic field magnitude and angular error δ like that shown in Fig. 13. Since we only use measurements where the magnetic field magnitude is greater than 10 nT, the direction error is always less than 17° while the data set's median magnetic field magnitude of 16.8 nT gives a median error of $\delta = 5.2°$ (see Fig. 13).

The second source is the curvature of magnetic field lines between the spacecraft and 185 km. This produces an effective angular error, denoted β, which depends on the average radius of curvature R_c, of the magnetic field and the straight line distance x from the spacecraft to 185 km altitude. Fig. 14 illustrates this for the case where the magnetic elevation angle

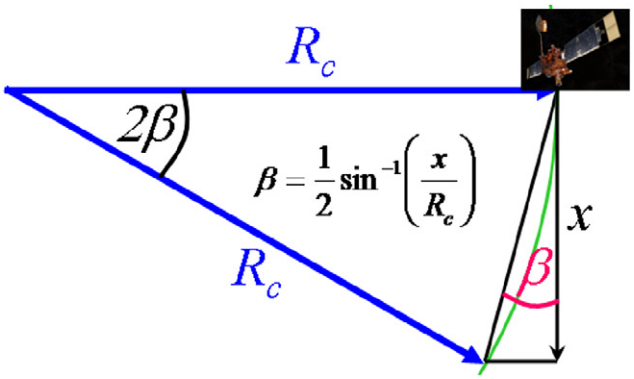

Fig. 14. Illustration showing the effective angular error β in the field line tracing resulting from the curvature of radius R_c of the magnetic field line (shown in light green).

is 90° (i.e. radial field lines), which gives our best estimate for β since we have no information as to which direction the magnetic field curves. β is thus given by the expression:

$$\beta = \frac{1}{2}\sin^{-1}\left(\frac{x}{R_c}\right). \tag{D.2}$$

These angular errors δ, β add in three-dimensional space and their sum γ depends on their relative orientation, i.e. the azimuth angle ϕ of one with respect to the other:

$$\cos\gamma = \cos\beta\cos\delta + \sin\beta\cos\phi\sin\delta. \tag{D.3}$$

However, since we cannot know this azimuth angle, we average over all values of ϕ from 0° to 360°, the cosine in the second term in Eq. (D.3) then averages to zero and we are left with the mean value of γ, the total field line tracing angular error:

$$\bar{\gamma} = \cos^{-1}[\cos\beta\cos\delta]. \tag{D.4}$$

The geographic tracing error (in km) can now be calculated. Consider an assumed-straight magnetic field line of length x and elevation angle θ with respect to the horizontal, and its cone of uncertainty (of half opening angle γ), starting at the spacecraft and intersecting the absorption layer at 185 km. To a very good approximation, the cone's projection on the atmosphere is an ellipse, as illustrated in Fig. 15, whose semimajor axis a is given by:

$$a = \frac{x\sin 2\gamma\sin\theta}{2\sin(\theta+\gamma)\sin(\theta-\gamma)}. \tag{D.5}$$

The center line of the cone intersects the ellipse at one of the foci. The geographic tracing error is then given by the mean distance from this focus to the edge of the ellipse, averaged around the ellipse's circumference, which can easily be shown to be equal to the semimajor axis a (Eq. (D.5)).

We can now combine Eqs. (B.1), (D.1), (D.4), and (D.5) to examine how the theoretical geographic tracing error varies as a function of the field line curvature radius R_c and magnetic elevation angle θ, as color-plotted in Fig. 16. However, before we can use this plot to determine under what conditions we may reliably assume straight-line tracing of field lines, we need to estimate typical field line curvature radii that we are likely to

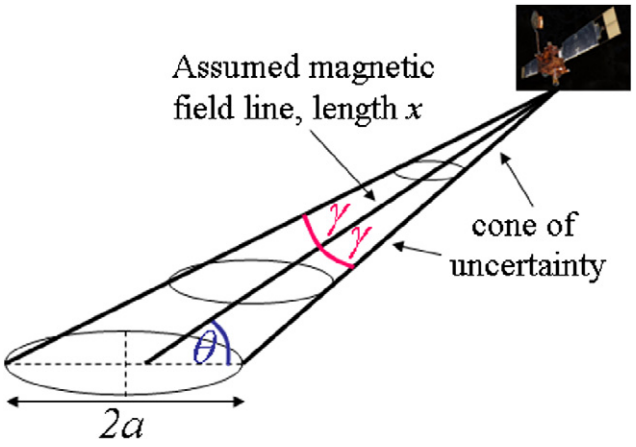

Fig. 15. Illustration showing the assumed magnetic field line with elevation angle θ, its cone of uncertainty of half angle γ, and the error ellipse resulting from the cone's projection on a flat surface.

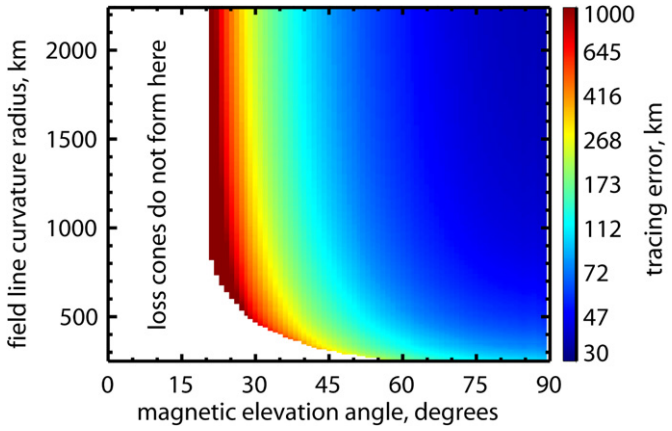

Fig. 16. Theoretical field line tracing error is color-plotted as a function of field line curvature and magnetic elevation angle. Loss cones do not form when the curvature is too great for the field line to intersect the electron absorption layer. The median instrumental field direction error (δ) of 12° and mean spacecraft altitude of ~400 km are assumed.

encounter in the data set. The curvature vector $\underline{\boldsymbol{\rho}}$ can be calculated from the magnetic field $\underline{\boldsymbol{B}}$ as follows (Parks, 2004, p. 125):

$$\frac{\vec{\rho}}{|\vec{\rho}|^2} = -\frac{\partial}{\partial s}\left(\frac{\vec{B}}{|\vec{B}|}\right), \tag{D.6}$$

where the distance variable s is along the magnetic field line. Fig. 17 plots the field line geometries, field magnitudes and field curvature radii in 2 dimensions resulting from the superposition of a crustal dipolar field and a constant external ambient field for two typical cases. The curvature radius along the field lines, averaged over the distance between the spacecraft and the absorption layer is typically greater than 500 km and often much greater. The only exceptions occur where the external field is oppositely directed to the crustal field, field lines diverge (e.g. left side of left panel of Fig. 17) and hence there is no magnetic reflection whatsoever. Cases where such 'masking' of crustal fields occurs will be excluded from the final map, as dealt with in Appendix E. Generally, weaker crustal fields produce less curvature than strong fields but the final map will show that crustal fields are stronger than the case shown in the left panels

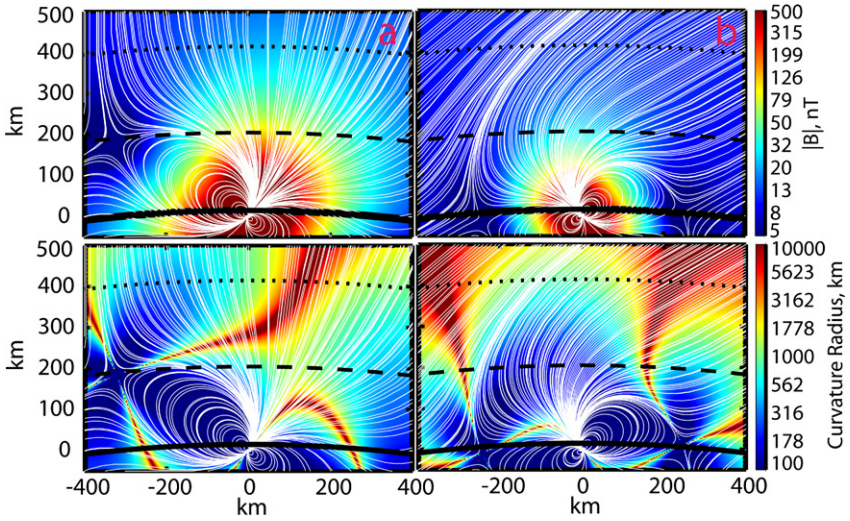

Fig. 17. Magnetic field magnitude (top panels) and field line curvature radii (bottom panels) are color-plotted on logarithmic scales with magnetic field lines (in white), resulting from 2 typical cases of a superposition of the field of a dipolar crustal source and a 12 nT constant external field, demonstrating how field line curvature affects tracing. The surface is represented by a thick solid black line, the absorption layer at 185 km altitude by a dashed black line and the spacecraft orbit at 400 km by a black dotted line.

of Fig. 17 for <2% of the planet's surface, which are regions where MAG measurements have already well-characterized the crustal fields and so ER measurements are less important.

We now turn back to Fig. 16 and notice that the tracing error increases sharply from ∼125 km to >400 km with an elevation angle decrease of ∼10°. This sharp increase occurs between 30° and 45° depending on curvature radius. With 500 km as our typical lower bound for curvature radius, we can exclude the overwhelming majority of cases with a tracing error greater than 150 km by excluding all those with elevation angles less than 40°. Once these are excluded, the data set's median absolute elevation angle of 58.5° implies a median tracing error of <100 km for most field line geometries.

The purpose of the analysis in this section has been to define a cutoff value of magnetic elevation angle (40°) below which we cannot trust the straight field line approximation to deliver an accurate geographic location for the crustal field at 185 km.

Appendix E. Correcting for masking of crustal fields

We have already mentioned that the magnetic field in the near-Mars nightside environment can be well approximated by a vector sum of the unchanging crustal field and the temporally variable double-lobed induced magnetotail field (Acuña et al., 2001). However, our parameterization of the magnetic profile (Eq. (1)) is necessarily a scalar one because the electron reflectometry method is sensitive only to magnetic field magnitudes. It implicitly assumes that the magnetotail or 'ambient' field vector $\underline{\boldsymbol{B_a}}$ and the crustal field vector $\underline{\boldsymbol{B_c}}$ can be added as scalar quantities, i.e. that they are co-linear. Of course, this is generally not the case as they can have any relative orientation, an illustration of which is shown in Fig. 18.

Thus, with our necessary assumption that their separation angle η is zero, we calculate B_{185} as follows:

$$B_{185} = |\vec{B}_{\rm tot}| - |\vec{B}_a|, \tag{E.1}$$

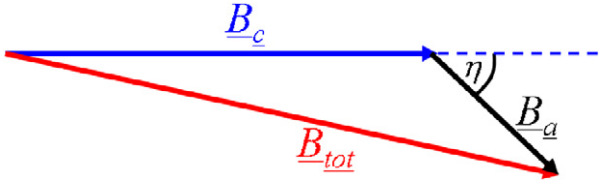

Fig. 18. Illustration of the vector relationship between the crustal field B_c, the ambient field B_a and the resultant total field $B_{\rm tot}$ in terms of the angle η between B_c and B_a.

whereas in fact, according to the cosine rule, the crustal field magnitude B_c is given:

$$B_c = -B_a \cos\eta \pm \sqrt{B_a^2 \cos^2\eta + \left(B_{\rm tot}^2 - B_a^2\right)}, \tag{E.2}$$

where B_a and $B_{\rm tot}$ are the magnitudes of the ambient and total fields respectively, with '+' appropriate for $B_{\rm tot} > B_a$ and '−' for $B_{\rm tot} < B_a$. So, depending on the relative orientation of $\underline{\boldsymbol{B_a}}$ and $\underline{\boldsymbol{B_c}}$, the ambient field can partially or totally 'mask' the crustal field. The result is that we underestimate B_{185} by an amount $\Delta B_{185\text{-mask}}$:

$$\Delta B_{185\text{-mask}} = B_a(1 - \cos\eta) - B_{\rm tot} \pm \sqrt{B_a^2 \cos^2\eta + \left(B_{\rm tot}^2 - B_a^2\right)}. \tag{E.3}$$

We solve for $B_{\rm tot}$ from each loss cone and also obtain a reasonable estimate of the true B_a by solving for $B_a/B_{\rm sc}$, despite its correlation with p (see Fig. 12), although B_a is always $<B_{\rm tot}$ in our parameterization. However, to estimate $\Delta B_{185\text{-mask}}$, we further require a method for estimating or at least constraining η. In this regard, it helps to remember in that the vector $\underline{\boldsymbol{B_c}}$ at 185 km is unknown but constant, whereas the vector $\underline{\boldsymbol{B_a}}$ is variable but its direction can be estimated reasonably well by assuming that it is equal to the average direction of the 10 nearest-in-time magnetic field vectors measured when the spacecraft was in a geographic region of no discernible crustal magnetic field (i.e. $B_{185} < 4$ nT). Thus, for every value of B_{185},

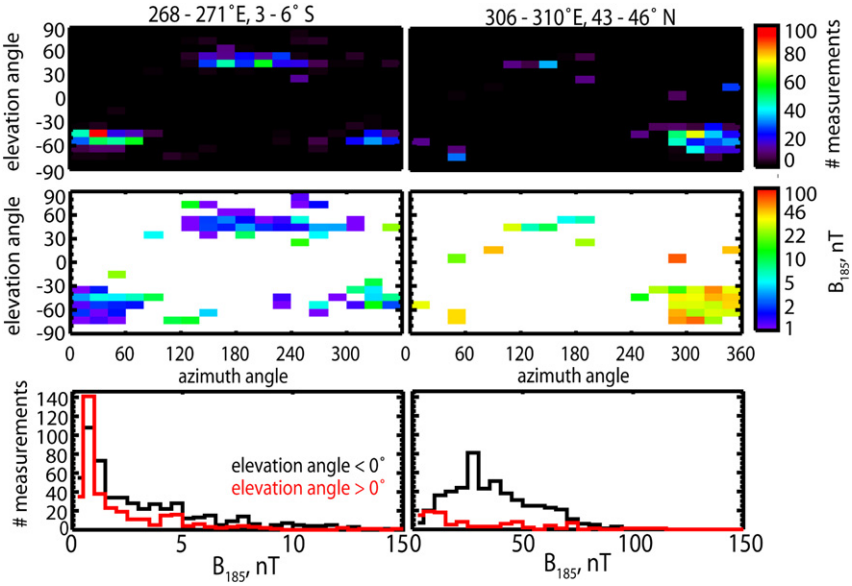

Fig. 19. For ∼200 × 200 km regions of very weak (left) and moderate (right) crustal magnetic field, the number of measurements (top panels) and mean value of B_{185} (middle panels) are plotted versus estimated ambient (i.e. noncrustal) field elevation angle and azimuth angle in 10° × 20° bins. The bottom panels are histograms of B_{185}, split into measurements with positive (black) and negative (red) elevation angles.

we have an associated estimate for the elevation and azimuth angles of the external ambient field. As the spacecraft passes over the same crustal magnetic field region many hundreds of times at 2 a.m., we can build up a picture of which directions of $\underline{\boldsymbol{B_a}}$ are most prevalent and how B_{185} changes with this direction.

We find that, in very weak crustal field regions at least 500 km away from strong fields, the ambient field typically lies in one of two nearly opposite directions (see Fig. 19, left column), matching what we would expect from a sunward/anti-sunward double-lobed nightside magnetotail (Halekas et al., 2006). However, as we approach stronger field regions, loss cones increasingly form preferentially for one ambient field direction over the other (see Fig. 19, right column), likely due to the differences in magnetic topology that result from the superpositions of the permanent crustal field and the bipolar angular distribution of the ambient field. We also find that derived values of B_{185} are in almost all cases higher for the range of elevation angles in which there are more measurements. Now it is clear from Fig. 18 that $|\underline{\boldsymbol{B_{tot}}}|$, and hence B_{185}, reaches a maximum with respect to elevation angle when η is closest to zero and a minimum when η is closest to 180°. Therefore, we may assume that $\eta < 90°$ if we consider only measurements for which the ambient elevation angle is positive or negative, depending which polarity contains the higher average value of B_{185}. As mentioned above, this will nearly always be the polarity with the majority of measurements, which is not surprising because some degree of co-linearity of the crustal and external fields should give the incident electrons a direct path into the atmosphere against a magnetic gradient, which is a required condition for loss cone formation.

Since there are usually not enough measurements with both polarities to attempt to find a stricter constraint on η, we will simply assume that it takes a random value between 0° and 90°

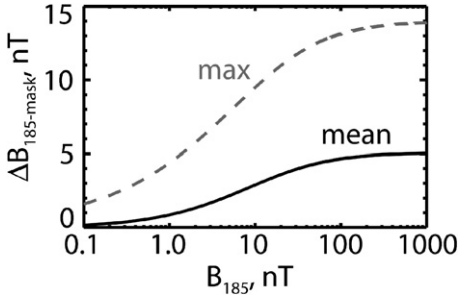

Fig. 20. The mean and maximum amount by which B_{185} is underestimated, $\Delta B_{185\text{-mask}}$, is plotted versus B_{185}. The data set median value of B_a (13.5 nT) is assumed.

for all the values of B_{185} that we will use. This allows us to calculate both a mean and maximum value of $\Delta B_{185\text{-mask}}$ for a given measurement of B_{185}:

$$\bar{\Delta}\,\bar{B}_{185\text{-mask}} = \frac{2}{\pi}\int_0^{\pi/2} \Delta B_{185\text{-mask}}(\eta)\,\mathrm{d}\eta,$$

$$\max(\Delta B_{185\text{-mask}}) = \sqrt{B_{\text{tot}}^2 - B_a^2} + B_a - B_{\text{tot}}. \tag{E.4}$$

Therefore, the first correction we make to the data set is to increase every derived value of B_{185} by the mean value of $\Delta B_{185\text{-mask}}$. Fig. 20 shows how both the mean and maximum values of $\Delta B_{185\text{-mask}}$ vary with B_{185}.

Appendix F. Determining the most likely value of B_{185} from data distributions

Next we address the issue of how to determine the most likely value of B_{185} in a given geographic region of Mars from the distribution of measurements. The simplest method would

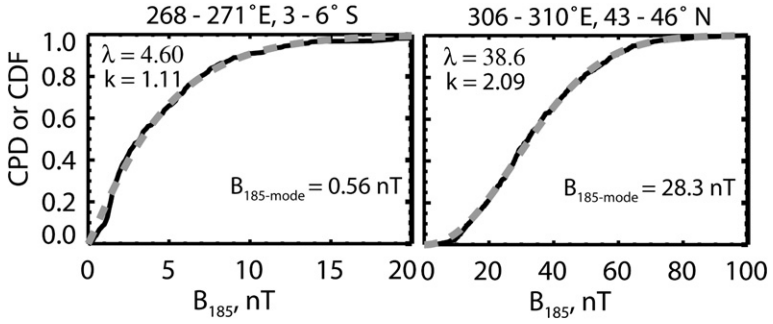

Fig. 21. Cumulative probability distributions of masking-corrected values of B_{185} in the indicated geographic regions, are plotted with a solid black line. Best fit Weibull cumulative distribution functions are plotted with a dotted gray line.

be to simply take the mean of all the measurements. However, this would implicitly assume that the distributions are Gaussian, which is clearly not the case, both because the measurements can never be negative and because they simply do not appear Gaussian, as shown in Fig. 19 (bottom panels). The theoretical distribution that best suits the data distributions is the Weibull distribution (e.g. Johnson et al., 1995), a positive-only, 2-parameter distribution whose probability density function f and cumulative distribution function (CDF) are given by:

$$f(x|\lambda,k) = \frac{k}{\lambda}\left(\frac{x}{\lambda}\right)^{k-1}\exp\left[-\left(\frac{x}{\lambda}\right)^{k}\right],$$
$$\mathrm{CDF}(x|\lambda,k) = 1-\exp\left[-\left(\frac{x}{\lambda}\right)^{k}\right], \quad \text{(F.1)}$$

where λ has the dimension of x and k is dimensionless. We choose it because its flexibility allows us to adequately describe the distributions in (a) the very weakest crustal field regions (e.g. left side of Fig. 19), where the measurements are mostly random positive fluctuations from close to zero and where the tail of the distribution varies as $\sim\exp(-1/B_{185})$, i.e. $k\sim 1$, in (b) the moderate field regions (e.g. right side of Fig. 19) where the distributions have a well-defined peak away from zero and are best described by a Rayleigh distribution (i.e. $k\sim 2$), in (c) strong field regions where the distribution becomes comparatively wider with $k\sim 3.0$–4.0 and in all cases between.

We fit the cumulative probability distributions (CPDs, i.e. the fraction of measurement values greater than x) of the data to the Weibull CDF, because the CPD requires fewer data points to characterize than the raw probability distribution and takes values between 0 and 1, making fitting more straightforward. By minimizing χ^2, we solve for the most likely values of λ and k. Two of such fitted CDFs, for the same geographic regions as Fig. 19 and corrected for masking, are shown in Fig. 21. It is clear that the data and fitted curves are a very good match in both cases, illustrating the suitability of the Weibull distribution for this purpose. We are primarily interested in the most likely value of B_{185}, i.e. the mode of the distribution. In the Weibull case, this is given by:

$$B_{185\text{-mode}} = \lambda\left(1-\frac{1}{k}\right)^{1/k}. \quad \text{(F.2)}$$

In cases where the number of measurements is not sufficient to fit reliably (say, <30) or in the tiny fraction of cases (<0.2%) where the fit either doesn't converge or results in an obviously incorrect answer (e.g. <3 nT when the median value is greater than 200 nT), we resort to the following empirical technique. By inserting Eq. (F.2) into the expression for the CDF in Eq. (F.1), we see that $B_{185\text{-mode}}$ occurs at $\mathrm{CDF}_{\mathrm{mode}}$ where $\mathrm{CDF}_{\mathrm{mode}} = 1-\exp(1/k-1)$. For the well-fitted distributions, we find that the value of k scales approximately with the fourth root of the median value of B_{185}, holding true from <1 nT to ~500 nT. Thus, we calculate $\mathrm{CDF}_{\mathrm{mode}}$ and simply interpolate to find the value of B_{185} where the CPD intersects $\mathrm{CDF}_{\mathrm{mode}}$. As for error estimates for B_{185}, rather than using the fitted uncertainties from each CPD (which we don't always obtain), we instead use the difference between values of $B_{185\text{-mode}}$ from each half of the mission (see Section 4.4).

Appendix G. Improvements over the ER map of Mitchell et al. (2007)

Most of Section 2, all of Section 3 and all Appendices A–F (with the exception of approximately half of Appendix C) describe many of the corrections or improvements to the method or analysis of results not considered when the Mitchell et al. manuscript was prepared in 2004–2005. They are summarized below, along with additional improvements not mentioned elsewhere:

1. The atmospheric neutral density profile assumed is based upon mean neutral atmospheric densities measured with the ER density probing technique described in Lillis et al. (2008b) instead of a somewhat arbitrarily chosen 2 a.m. solar EUV medium, equatorial, equinox MTGCM atmosphere. Coincidentally, because the mean atmosphere turns out to be so close to this previously assumed atmosphere, the effect of this change is almost negligible (Appendix A).
2. A more precise equation (Eq. (6.2) of Lillis et al., 2006) is used to relate distance from magnetized crust to altitude above planet. The previous version omitted the altitude h in the denominator of both major terms resulting in unintended path length errors of a few percent.
3. Argon is added to the list of atmospheric gases (CO_2, O, O_2, N_2, CO) considered previously using the cross-sections contained in Chilton and Lin (1999), Panajotovic et al. (1997) and Ajello et al. (1990). Argon is a relatively minor

species (Nier and McElroy, 1977), making this an incremental improvement (Lillis et al., 2008a).

4. Improved cross-sections for electron impact with CO_2, taken from Itikawa (2002), reflecting new laboratory measurements, were used, instead of those contained in the compilation of Sung and Fox (2000).
5. Loss cone measurements in 3 energy channels spanning ∼90–400 eV are analyzed, providing additional statistical confidence, compared with one channel (∼148–245 eV) used in the production of the Mitchell et al. map.
6. The presence of electrostatic potentials is accounted for in the fitting of the loss cones and derived crustal magnetic field values are thus corrected. Such potentials are stronger in strong field regions (Lillis et al., 2006) but their polarity varies substantially on a local scale, so the effect on the magnetic map of correcting for the potentials is to raise derived field values in certain regions and lower them in others.
7. The mean altitude of greatest sensitivity, 185 km, was calculated using the correct formalism outlined in Appendix B and explained in detail in Lillis et al. (2008a). The previous quoted altitude in Mitchell et al. (2007), 170 km, was derived using a simplistic range calculation and, though it is not too far from the true value, the current analysis shows that loss cone shapes have a factor of ∼4 lower sensitivity to crustal magnetic fields at that altitude (Appendix B).
8. The error in assuming straight magnetic field lines for the purposes of tracing measurements from ∼400 km to ∼200 km is correctly evaluated and data for which this error is unacceptably large have been excluded (Appendix D). This was not previously considered at all.
9. The masking of crustal magnetic fields by external, induced magnetic fields is correctly treated and the data has been corrected for this effect insofar as possible using multiple measurements with different external field orientations (Appendix E). This was also not previously considered.
10. The most likely value of B_{185} in a given geographic sector is calculated more appropriately using the mode of the best fit to a Weibull distribution which, for the observed distributions which are positive-definite, is far more appropriate than the previously considered fit to a Gaussian distribution (Appendix F). This especially makes a difference for very weak field regions, where crustal field values had been overestimated by up to factors of several.
11. The map presented in this article is constructed from data collected from 04/1999 to 08/2006. It contains 33 months of additional data and thus has better statistical confidence than the previous map in Mitchell et al. (2007).

References

Abramov, O., Kring, D.A., 2004. Impact-induced hydrothermal system at the Sudbury crater: Duration, temperatures, mechanics, and biological implications. Lunar Planet. Sci. D 35. Abstract 1697.

Acuña, M.H., and 16 colleagues, 1992. The Mars Observer magnetic fields investigation. J. Geophys. Res. Planets 97, 7799–7814.

Acuña, M.H., and 19 colleagues, 1998. Magnetic field and plasma observations at Mars: Initial results of the Mars Global Surveyor mission. Science 279, 1676–1680.

Acuña, M.H., and 12 colleagues, 1999. Global distribution of crustal magnetization discovered by the Mars Global Surveyor MAG/ER experiment. Science 284, 790–793.

Acuña, M.H., and 13 colleagues, 2001. Magnetic field of Mars: Summary of results from the aerobraking and mapping orbits. J. Geophys. Res. 106, 23403–23417.

Ajello, J.M., James, G.K., Franklin, B., Howell, S., 1990. Study of electron impact excitation of argon in the extreme ultraviolet: Emission cross-section of resonance lines of Ar I, Ar II. J. Phys. B At. Mol. Opt. Phys. 23, 4355–4376.

Anderson, K.A., Lin, R.P., McCoy, J.E., McGuire, R.E., 1976. Measurements of lunar and planetary magnetic fields by reflection of low energy electrons. Space Sci. Instrum. 1, 439–470.

Arkani-Hamed, J., 2001a. A 50-degree spherical harmonic model of the magnetic field of Mars. J. Geophys. Res. 106, 23197–23208.

Arkani-Hamed, J., 2001b. Paleomagnetic pole positions and pole reversals of Mars. Geophys. Res. Lett. 28, 3409–3412.

Arkani-Hamed, J., 2002a. Magnetization of the martian crust. J. Geophys. Res. 107, doi:10.1029/2001JE001496.

Arkani-Hamed, J., 2002b. An improved 50-degree spherical harmonic model of the magnetic field of Mars derived from both high-altitude and low-altitude datasets. J. Geophys. Res. 107, doi:10.1029/2001JE001835.

Arkani-Hamed, J., 2003. Thermoremanent magnetization of the martian lithosphere. J. Geophys. Res. 108, doi:10.1029/2003JE002049.

Arkani-Hamed, J., 2004. A coherent model of the crustal field of Mars. J. Geophys. Res. 109, doi:10.1029/2003JE002265.

Arkani-Hamed, J., 2005. Magnetic crust of Mars. J. Geophys. Res. 110, doi:10.1029/2004JE002397. E08005.

Arkani-Hamed, J., Boutin, D., 2004. Paleomagnetic poles of Mars: Revisited. J. Geophys. Res. 109, doi:10.1029/2003J3002229.

Bacon, C.R., 1982. Time-predictable biomodal volcanism in the Coso Range, California. Geology 10, 65–69.

Bandfield, J.L., 2006. Extended surface exposures of granitoid compositions in Syrtis Major, Mars. Geophys. Res. Lett. 33, doi:10.1029/2005GL025559. L06203.

Behrendt, J.C., Finn, C.A., Blankenship, D., Bell, R.E., 1998. Aeromagnetic evidence for a volcanic caldera complex beneath the divide of the West Antarctic Ice Sheet. Geophys. Res. Lett. 25, 4385–4388.

Bertucci, C., and 11 colleagues, 2003. Magnetic field draping enhancement at the martian magnetic pileup boundary from Mars global surveyor observations. Geophys. Res. Lett. 30 (2), doi:10.1029/2002GL015713. 1099.

Blackwell, D.D., Steele, J.L., Kelley, S., Korosec, M.A., 1990. Heat flow in the state of Washington and thermal conditions in the Cascade Range. J. Geophys. Res. 95, 19495–19516.

Blakely, R.J., 1995. Potential Theory in Gravity and Magnetic Applications. Cambridge Univ. Press, Cambridge, UK.

Bougher, S.W., Engle, S., Roble, R.G., Foster, B., 1999. Comparative terrestrial planet thermospheres. 2. Solar cycle variation of global structure and winds at equinox. J. Geophys. Res. 104, 16591–16611.

Brain, D.A., Bagenal, F., Acuña, M.H., Connerney, J.E.P., 2003. Martian magnetic morphology: Contributions from the solar wind and crust. J. Geophys. Res. 108. 8-1.

Brain, D.A., Halekas, J.S., Peticolas, L.M., Lin, R.P., Luhmann, J.G., Mitchell, D.L., Delory, G.T., Bougher, S.W., Acuña, M.H., Réme, H., 2006. On the origin of aurorae on Mars. Geophys. Res. Lett. 33. 1201.

Cain, J.C., Ferguson, B.B., Mozoni, D., 2003. An $n = 90$ internal potential function of the martian crustal magnetic field. J. Geophys. Res. 107, doi:10.1029/2000JE001487.

Carporzen, L., Gilder, S.A., Hart, R.J., 2005. Paleomagnetism of the Vredefort meteorite crater and implications for craters on Mars. Nature 435, 198–201.

Chilton, J.E., Lin, C.C., 1999. Measurement of electron-impact excitation into the $3p^5 3d$ and $3p^5 5s$ levels of argon using Fourier-transform spectroscopy. Phys. Rev. A 60 (5), 3712–3721.

Connerney, J.E.P., Acuña, M.H., Wasilewski, P.J., Ness, N.F., Réme, H., Mazelle, C., Vignes, D., Lin, R.P., Mitchell, D.L., Cloutier, P.A., 1999. Magnetic lineations in the ancient crust of Mars. Science 284, 794–798.

Connerney, J.E.P., Acuña, M.H., Wasilewski, P.J., Ness, N.F., Reme, H., Mazelle, C., Vignes, D., Lin, R.P., Mitchell, D.L., 2001. The global magnetic field of Mars and implications for crustal evolution. Geophys. Res. Lett. 28, 4015–4018.

Crisp, J.A., 1984. Rates of magma emplacement and volcanic output. J. Volcanol. Geotherm. Res. 20, 177–211.

Crown, D.A., Greeley, R., 1993. Volcanic geology of Hadriaca Patera and the eastern Hellas region of Mars. J. Geophys. Res. 98, 3431–3451.

Daubar, I.J., Kring, D.A., 2001. Impact-induced hydrothermal systems: Heat sources and lifetimes. Lunar Planet. Sci. 32. Abstract 1727.

Ernst, R.E., Grosfils, E.B., Mege, D., 2001. Giant dike swarms: Earth, Venus, and Mars. Annu. Rev. Earth Planet. Sci. 29, 489–534.

Ferguson, B.B., Cain, J.C., Crider, D.H., Brain, D.A., Harnett, E.M., 2005. External fields on the nightside of Mars at Mars Global Surveyor mapping altitudes. Geophys. Res. Lett. 32 (16), doi:10.1029/2004GL021964.

Frey, H.V., 2006. Impact constraints on, and a chronology for, major events in early Mars history. J. Geophys. Res. 111, doi:10.1029/2005JE002449. E08S91.

Greeley, R., Schneid, B.D., 1991. Magma generation on Mars: Amounts, rates, and comparisons with Earth, Moon and Venus. Science 254, 996–998.

Gregg, T.K.P., Farley, M.A., 2006. Mafic pyroclastic flows at Tyrrhena Patera, Mars: Constraints from observations and models. J. Volcanol. Geotherm. Res. 155, 81–89.

Hiesinger, H., Head, J.W., 2004. The Syrtis Major volcanic province, Mars: Synthesis from Mars Global Surveyor data. J. Geophys. Res. 109, doi:10.1029/2003JE002143. E01004.

Halekas, J.S., Brain, D.A., Lillis, R.J., Fillingim, M.O., Mitchell, D.L., Lin, R.P., 2006. Current sheets at low altitudes in the martian magnetotail. Geophys. Res. Lett. 33 (13), doi:10.1029/2006GL026229.

Hartmann, W.K., Neukum, G., 2001. Cratering chronology and the evolution of Mars. Space Sci. Rev. 96, 165–194.

Hood, L.L., Zakharian, A., 2001. Mapping and modeling of magnetic anomalies in the northern polar region of Mars. J. Geophys. Res. 106 (E7), 14601–14619.

Hood, L.L., Richmond, N.C., Pierazzo, E., Rochette, P., 2003. Distribution of crustal magnetic fields on Mars: Shock effects of basin-forming impacts. Geophys. Res. Lett. 30 (6), doi:10.1029/2002GL016657.

Hood, L.L., Young, C.N., Richmond, N.C., Harrison, K.P., 2005. Modeling of major martian magnetic anomalies: Further evidence for polar reorientations during the Noachian. Icarus 177, 144–173.

Ingebritsen, S.E., Mariner, R.H., Sherrod, D.R., 1994. Hydrothermal systems of the Cascades Range, North-Central Oregon. USGS Prof. Pap. 1044-L, 86 pp.

Itikawa, Y., 2002. Cross-sections for electron collisions with carbon dioxide. J. Phys. Chem. Ref. Data 31 (3), 749–768.

Johnson, C.L., Phillips, R.J., 2005. Evolution of the Tharsis region of Mars: Insights from magnetic field observations. Earth Planet. Sci. Lett. 230, 241–254.

Johnson, N., Kotz, S., Balakrishnan, N., 1995. Continuous Univariate Distributions, vol. 2, second ed. Wiley, New York.

Kiefer, W.S., 2004. Gravity evidence for an extinct magma chamber beneath Syrtis Major, Mars: A look at the magmatic plumbing system. Earth Planet. Sci. Lett. 222, 349–361.

Langlais, B., Purucker, M.E., Mandea, M., 2004. Crustal magnetic field of Mars. J. Geophys. Res. 109, doi:10.1029/2003JE002048.

Leonard, G.J., Tanaka, K.L., 2001. Geologic map of the Hellas region of Mars. US Geological Survey Geologic Investigations Series I-2694, pamphlet 10 p., 1 plate, scale 1:4,336,000, http://pubs.usgs.gov/imap/i2694/.

Lillis, R.J., Mitchell, D.L., Lee, C.O., Lin, R.P., Reme, H., Cloutier, P.A., Acuña, M.H., 2003. High sensitivity mapping of crustal magnetic field on Mars with electron reflectometry. Geophys. Res. Abstr. 5. 07993.

Lillis , R.J., Mitchell, D.L., Lin, R.P., Connerney, J.E.P., Acuña, M.H., 2004. Mapping crustal magnetic fields at Mars using electron reflectometry. Geophys. Res. Lett. 31, doi:10.1029/2004GL020189. L15702.

Lillis, R.J., Manga, M., Mitchell, D.L., Lin, R.P., Acuña, M.H., 2006. Unusual magnetic signature of the Hadriaca Patera Volcano: Implications for early Mars. Geophys. Res. Lett. 33, doi:10.1029/2005GL024905. L03202.

Lillis, R.J., Mitchell, D.L., Lin, R.P., Acuña, M.H., 2008a. Electron reflectometry in the martian atmosphere. Icarus 194, 544–561.

Lillis, R.J., Bougher, S.W., Mitchell, D.L., Brain, D.A., Lin, R.P., Acuña, M.H., 2008b. Continuous monitoring of night side upper thermospheric mass densities in the martian southern hemisphere over 4 martian years using electron reflectometry. Icarus 194, 562–574.

Lin, R.P., 1979. High spatial resolution measurements of surface magnetic fields of the lunar frontside. Proc. Lunar Sci. Conf. 10, 2259–2264. A80-23677 08-91.

Maia, M., Dyment, J., Jouannetaud, D., 2005. Constraints on age and construction process of the Foundation chain submarine volcanoes from magnetic modeling. Earth Planet. Sci. Lett. 235, 183–199.

Meyer, B.R., Gregg, T.K.P., 2001. Inferring lava flow-field emplacement using MOLA: Topography of Tyrrhena Patera's flow field. Lunar Planet. Sci. 32. Abstract 1849.

Mitchell, D.L., Lin, R.P., Mazelle, C., Rème, H., Cloutier, P.A., Connerney, J.E.P., Acuña, M.H., Ness, N.F., 2001. Probing Mars' crustal magnetic field and ionosphere with the MGS Electron Reflectometer. J. Geophys. Res. 106, 23419–23427.

Mitchell, D.L., Lillis, R.J., Lin, R.P., Connerney, J.E.P., Acuña, M.H., 2007. A global map of Mars' crustal magnetic field based on electron reflectometry. J. Geophys. Res. 112 (E1), doi:10.1029/2005JE002564. E01000.

Nier, A.O., McElroy, M.B., 1977. Composition and structure of Mars' upper atmosphere—Results from the neutral mass spectrometers on Viking 1 and 2. J. Geophys. Res. 82, 4341–4349.

Nimmo, F., Gilmore, M.S., 2001. Constraints on the depth of magnetized crust on Mars from impact craters, 2. J. Geophys. Res. 106, 12315–12323.

Ogawa, Y., Manga, M., 2007. Thermal demagnetization of martian upper crust by magma intrusion. Geophys. Res. Lett. 34 (16), doi:10.1029/2007GL030565. 16302.

O'Neill, C., Lenardic, A., Jellinek, A.M., Kiefer, W.S., 2007. Melt propagation and volcanism in mantle convection simulations, with applications for martian volcanic and atmospheric evolution. J. Geophys. Res. 112, doi:10.1029/2006JE002799. E07003.

Panajotovic, R., Filipovic, D., Marinkovich, P., Pejcev, V., Kurepa, M., Vuskovic, L., 1997. Critical minima in elastic scattering by argon. J. Phys. B At. Mol. Opt. Phys. 30, 5877–5894.

Parks, G., 2004. Physics of Space Plasmas. Westview, Cambridge, MA. 125 pp.

Plescia, J.B., 2004. Morphometric properties of martian volcanoes. J. Geophys. Res. 109, doi:10.1029/2002JE002031. E03003.

Press, W.H., Teukolsky, S.A., Vetterling, W.T., Flannery, B.P., 1992. Numerical Recipes in C: The Art of Scientific Computing. Cambridge.

Purucker, M.E., Ravat, D., Frey, H., Voorhies, C., Sabaka, T., Acuna, M.H., 2000. An altitude-normalized magnetic map of Mars and its interpretation. Geophys. Res. Lett. 27, 2449–2452.

Shahnas, H., Arkani-Hamed, J., 2007. Viscous and impact demagnetization of martian crust. J. Geophys. Res. 112, doi:10.1029/2005JE002424. E02009.

Sherrod, D.R., Smith, J.G., 1990. Quaternary extrusion rates of the Cascade Range, Northwestern United States and Southern British Columbia. J. Geophys. Res. 95, 19465–19474.

Smith, D.E., and 24 colleagues, 2001. Mars Orbiter Laser Altimeter: Experiment summary after the first year of global mapping of Mars. J. Geophys. Res. 106, 23689–23722.

Solomon, S.C., and 16 colleagues, 2005. New perspectives on ancient Mars. Science 307, 1214–1220.

Sung, K., Fox, J.L., 2000. Electron impact cross sections for use in modeling the ionospheres/thermospheres of the Earth and planets. Eos (Fall Suppl.) 81. SA52A-11.

Wadge, G., 1982. Steady state volcanism: Evidence from eruption histories of polygenetic volcanoes. J. Geophys. Res. 87, 4035–4049.

Whaler, K.A., Purucker, M.E., 2005. A spatially continuous magnetization model for Mars. J. Geophys. Res. 110 (E9), doi:10.1029/2004JE002393.

White, S.M., Crisp, J.A., Spera, F.J., 2006. Long term eruption rates and magma budgets. Geochem. Geophys. Geosyst. 7, doi:10.1029/2005GC001002. Q03010.

Williams, J.-P., Nimmo, F., 2004. Thermal evolution of the martian core: Implications for an early dynamo. Geology 32, 97–100.

Wilson, L., Mouginis-Mark, P.J., 2003. Phreatomagmatic explosive origin of Hrad Vallis, Mars. J. Geophys. Res. 108, doi:10.1029/2002JE001927.

Yuan, D.-N., Sjogren, W.L., Konopliv, A.S., Kucinskas, A.B., 2001. Gravity field of Mars: A 75th degree and order model. J. Geophys. Res. 106 (E10), 23377–23401.